


 Cite this: *RSC Adv.*, 2022, **12**, 35002

Combined DFT, SCAPS-1D, and wxAMPS frameworks for design optimization of efficient $\text{Cs}_2\text{BiAgI}_6$ -based perovskite solar cells with different charge transport layers

M. Khalid Hossain, ^{*a} A. A. Arnab, ^b Ranjit C. Das, ^c K. M. Hossain, ^d M. H. K. Rubel, ^d Md. Ferdous Rahman, ^e H. Bencherif, ^f M. E. Emetere, ^g Mustafa K. A. Mohammed ^h and Rahul Pandey ⁱ

In this study, combined DFT, SCAPS-1D, and wxAMPS frameworks are used to investigate the optimized designs of $\text{Cs}_2\text{BiAgI}_6$ double perovskite-based solar cells. First-principles calculations are employed to investigate the structural stability, optical responses, and electronic contribution of the constituent elements in $\text{Cs}_2\text{BiAgI}_6$ absorber material, where SCAPS-1D and wxAMPS simulators are used to scrutinize different configurations of $\text{Cs}_2\text{BiAgI}_6$ solar cells. Here, PCBM, ZnO , TiO_2 , C_{60} , IGZO, SnO_2 , WS_2 , and CeO_2 are used as ETL, and Cu_2O , CuSCN , CuSbS_2 , NiO , P3HT, PEDOT:PSS, spiro-MeOTAD, Cul, CuO , V_2O_5 , CBTS, CFTS are used as HTL, and Au is used as a back contact. About ninety-six combinations of $\text{Cs}_2\text{BiAgI}_6$ -based solar cell structures are investigated, in which eight sets of solar cell structures are identified as the most efficient structures. Besides, holistic investigation on the effect of different factors such as the thickness of different layers, series and shunt resistances, temperature, capacitance, Mott–Schottky and generation–recombination rates, and J – V (current–voltage density) and QE (quantum efficiency) characteristics is performed. The results show CBTS as the best HTL for $\text{Cs}_2\text{BiAgI}_6$ with all eight ETLs used in this work, resulting in a power conversion efficiency (PCE) of 19.99%, 21.55%, 21.59%, 17.47%, 20.42%, 21.52%, 14.44%, 21.43% with PCBM, TiO_2 , ZnO , C_{60} , IGZO, SnO_2 , CeO_2 , WS_2 , respectively. The proposed strategy may pave the way for further design optimization of lead-free double perovskite solar cells.

Received 25th October 2022
 Accepted 28th November 2022

DOI: 10.1039/d2ra06734j
rsc.li/rsc-advances

1 Introduction

The depletion of energy sources and consumption of fossil fuels, natural gas, coal, *etc.*, have a negative impact on our society and environment.^{1–5} Therefore, developing alternative energy resources and sustainable energy sources with few economic and environmental concerns are the center of research worldwide.^{6–8} A solar cell is one of the most potential renewable and sustainable energy sources to attain the increasing energy demand and mitigate global warming.⁶ In recent years, perovskite solar cells (PSCs) have attracted significant research attention as a new approach in solar photovoltaic (PV) technology due to their significant power conversion efficiency (PCE) improvement from 3.8% to 25.2% since 2009.^{9,10} The general formula of PSCs is ABX_3 , where A and B represent a monovalent cation (methylammonium or CH_3NH_3^+ , formamidinium or $\text{H}_2\text{NCHNH}_2^+$, Cs^+ , CHCH_3^+) and a divalent metal cation (Pb , Sn , Ti , Bi , Ag), respectively, while X represents a halogen anion (Cl^- , Br^- and I^-). Compared to the other PSCs, lead-halide and organic-inorganic hybrid PSCs have received enormous attention due to their higher power conversion

^aInstitute of Electronics, Atomic Energy Research Establishment, Bangladesh Atomic Energy Commission, Dhaka 1349, Bangladesh. E-mail: khalid.baec@gmail.com; khalid@kyudai.jp

^bDepartment of Electrical & Electronic Engineering, Ahsanullah University of Science and Technology, Dhaka 1208, Bangladesh

^cMaterials Science and Engineering, Florida State University, Tallahassee, FL 32306, USA

^dDepartment of Materials Science and Engineering, University of Rajshahi, Rajshahi 6205, Bangladesh

^eDepartment of Electrical and Electronic Engineering, Begum Rokeya University, Rangpur 5400, Bangladesh

^fHNS-RE2SD, Higher National School of Renewable Energies, Environment and Sustainable Development, Batna 05078, Algeria

^gDepartment of Physics and Solar Energy, Bowen University, Iwo 232101, Osun, Nigeria

^hRadiological Techniques Department, Al-Mustaqbal University College, Hillah 51001, Babylon, Iraq

ⁱVLSI Centre of Excellence, Chitkara University Institute of Engineering and Technology, Chitkara University, Punjab 140401, India



efficiency (PCE) of around 25%, which is comparable to the champion silicon solar cell that has a record PCE of 26.7%.^{11–13} Despite the outstanding performance of PSCs, two major challenges prevent them from commercial applications like the use of the toxic material lead and organic cations, which have a volatile and hygroscopic nature.¹⁴ Organic–inorganic hybrid PSCs are chemically unstable when exposed to oxygen, moisture, and high temperatures because the organic cations are hygroscopic and volatile.¹⁵ On the other hand, lead-based halide perovskite is a highly toxic and hazardous material that can cause severe health and environmental issues.^{16–20}

As a result, there is a growing demand for nontoxic lead-free PSCs, leading researchers to develop several lead-free perovskite materials. As an alternative to lead-based perovskites, Pb^{2+} has been replaced by various nontoxic elements, including bivalent Sn^{2+} and Ge^{2+} .²¹ However, Sn^{2+} and Ge^{2+} in lead-free PSCs demonstrate low stability due to oxidation.²¹ Also, Pb^{2+} has been replaced with heterovalent M^{3+} , such as Bi^{3+} , which is non-toxic, isoelectronic with Pb^{2+} , and stable semiconducting halides.²² Bismuth-based PSCs exhibit longer charge carrier diffusion lengths due to their lower intrinsic trap densities and defect states.²³ However, when a highly charged Bi^{3+} ion was added to the three-dimensional $\text{A}^{1+}\text{M}^{2+}\text{X}_3$ structure, the three-dimensional $\text{A}^{1+}\text{M}^{2+}\text{X}_3$ structure produced poor optoelectronic characteristics compared to the lead-based perovskite.^{24,25} To overcome these undesirable properties, the elpasolite structure, also known as the double perovskite structure, has been used by adding Bi^{3+} anion.²⁶ The general formula of elpasolite structure is $\text{A}_2\text{M}^{1+}\text{M}^{3+}\text{X}_6$, where A, X, M^{1+} , and M^{3+} stand for monovalent cation, halide anion (Br^- , Cl^- , I^-), inorganic cation (Cu^+ , Ag^+ , Au^+ , Na^+ , K^+ , Rb^+ , and In^+), and organic or inorganic cation (Bi^{3+} or Sb^{3+}), respectively.²⁶ Recent studies showed that Bi^{3+} -based double perovskites with monovalent cation Ag^{1+} are a very promising material for photovoltaic applications due to their desirable bandgap, comparable charge carrier effective masses, excellent photoluminescence lifetime, extended carrier recombination lifetimes, and high stability.^{27–33} McClure and his coworker reported that $\text{Cs}_2\text{AgBiBr}_6$ and $\text{Cs}_2\text{AgBiCl}_6$ have an excellent bandgap and high stability compared to the $\text{CH}_3\text{NH}_3\text{PbX}_3$.²⁶ However, $\text{Cs}_2\text{AgBiBr}_6$ and $\text{Cs}_2\text{AgBiCl}_6$ are exhibited low efficiency, as large charge carrier effective masses, low charge carrier transport capabilities, and high band gap (>2 eV),^{34–36} which make them unfit for solar cells. On the contrary, the $\text{Cs}_2\text{AgBiI}_6$ absorber exhibited a favorable band gap (1.12 eV), higher light absorbing capacities, and higher performance than $\text{Cs}_2\text{AgBiBr}_6$ and $\text{Cs}_2\text{AgBiCl}_6$ which makes it suitable for the PSC.^{37,38}

The performance and efficiency of the absorber can be optimized in PSCs by using a suitable electron transport layer (ETL) and a hole transport layer (HTL). The properties and type of layer material used in PSCs significantly impact stability and performance. When choosing an HTL for the PSCs, the material properties should be considered, including the valence band offset between absorber and HTL, hole mobility, and cost.³⁹ Researchers mostly used HTLs such as spiro-MeOTAD and PEDOT:PSS in PSCs due to their excellent tunability and processability.^{40,41} However, the challenges associated with these materials are the processing cost, poor conductivity and hole

transport, and stability.⁴² On the other hand, the ETL should have a conduction band offset between the absorber and ETL, compatible with other layers' high electron mobility, and cost efficiency.³⁹ The maximum PCE of 28.4% is exhibited when TiO_2 as ETL is used in PSCs with MASnI_3 as the absorber layer.⁴³ However, the rutile crystalline phase of TiO_2 , which needs to be processed at high annealing temperatures, is used for solar cell applications.^{44–51} In addition, mesoporous- TiO_2 as ETL causes PSC's environment stability to deteriorate when exposed to ultraviolet light.⁴⁴ However, the low atmospheric stability and high-temperature processing of TiO_2 constrained them as ETL from PSCs. So far, a few studies have been conducted to enhance the device performance by selecting HTL and ETL with absorber layers in PSCs.^{52,53} In our recent study, we reported that CsPbI_3 absorber layer-based device with CBTS as HTL exhibited PCE of 16.71%, 17.90%, 17.86%, 14.47%, 17.76%, 17.82% with PCBM, TiO_2 , ZnO , C_{60} , IGZO, WS_2 ETL respectively.¹⁴ Another study demonstrates that using SnO_2 as ETL and CuSCN as HTL with MAPbI_3 absorber demonstrated a high PCE of 27%.⁵² Therefore, more research needs to be done to investigate the device performance of PSCs for different ETL, HTL, and back contact metals with lead-free perovskite absorber layers, to outperform Shockley Queisser's (SQ) efficiency limit for a single solar cell.

The electronic properties such as band gap and band structure, density of states (DOS), and charge density distribution are crucial for the investigation of the electronic contribution of different elements in perovskites and other structural compounds.^{14,54,55} The state of a material system can be properly understood by exploring its physical properties. It can also identify a material's possible practical applications. Nowadays, researchers have been performing theoretical works to explore the physical properties of materials of interest *via* the density functional theory (DFT). According to reports,^{14,56–58} several halide perovskite materials exhibit intriguing physical characteristics including structural, electrical, optical, and mechanical characteristics that make them potential candidates for optoelectronic and photovoltaic operations. Recently, Hadi *et al.*⁵⁹ have investigated the structural, electronic, optical, and mechanical properties of lead-free cubic double perovskite-type $\text{Cs}_2\text{AgBiBr}_6$ using the DFT method. The indirect band gap of $\text{Cs}_2\text{AgBiBr}_6$ was reduced and switched to direct by making the compound disordered following the disordering of $\text{Ag}^+/\text{Bi}^{3+}$ cations by creating an antisite defect in the sublattice. This reduction of the band gap is responsible to enhance the optical absorption in the visible region and makes $\text{Cs}_2\text{AgBiBr}_6$ suitable for solar cell applications.⁵⁹ Besides, the electronic band structure of isostructural double perovskite halide $\text{Cs}_2\text{AgSbCl}_6$ has also been investigated by both the PBE and HSE approximations.⁶⁰ It was reported that $\text{Cs}_2\text{AgSbCl}_6$ has an indirect band gap of 1.40 eV (HSE)/2.35 eV (PBE). To the best of our knowledge, the theoretical research on various physical properties of our chosen double perovskite-type halide $\text{Cs}_2\text{AgBiI}_6$ is not reported yet. Therefore, it is necessary to discover the physical properties of $\text{Cs}_2\text{AgBiI}_6$ system using computational studies like DFT.

In the present study, the performance of the lead-free $\text{Cs}_2\text{AgBiI}_6$ halide PSC is investigated through the one-dimensional



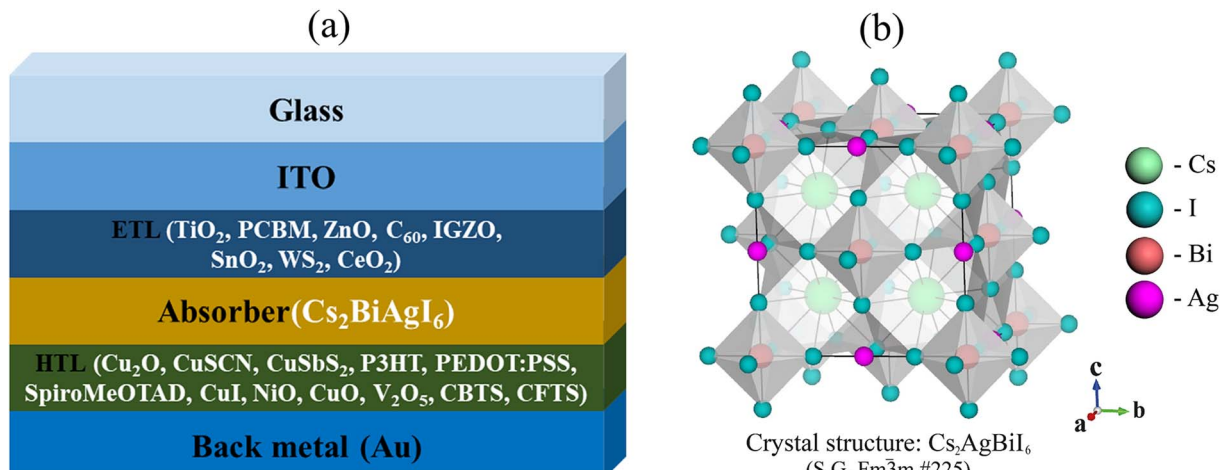


Fig. 1 (a) The design configuration of the $\text{Cs}_2\text{AgBiI}_6$ -based PSC, and (b) the crystal structure of the $\text{Cs}_2\text{AgBiI}_6$ cubic-single-perovskite semiconductor.

solar cell capacitance simulator (SCAPS-1D) platform for the very first time using numerous ETLs and HTLs. During the study, the performance is evaluated through TiO_2 , PCBM, ZnO , C_{60} , IGZO, SnO_2 , WS_2 , CeO_2 as ETL, and Cu_2O , CuSCN , CuSbS_2 , NiO , P3HT, PEDOT:PSS, spiro-MeOTAD, CuI , CuO , V_2O_5 , CBTS, CFTS as HTL with gold (Au) as back contact metal (Fig. 1(a)). Furthermore, the band gap of the $\text{Cs}_2\text{BiAgI}_6$ double perovskite absorber is also validated using theoretical first-principle calculations *via* the DFT framework together with the investigation of its structural and optical properties for the first time. In addition, we investigated the performance of the ETL and HTL layer along with the effect of absorber and ETL thickness, series resistance, shunt resistance, working temperature, capacitance and Mott–Schottky, generation and recombination rate, and current–voltage density (J – V) and quantum efficiency (QE) characteristics. Finally, the performance of the best configurations was verified through wxAMPS (widget-provided analysis of microelectronic and photonic structures) simulation findings.

2 Materials and methodology

2.1 First principal calculations of $\text{Cs}_2\text{BiAgI}_6$ absorber using DFT

This study performs the first-principle calculations exploiting the Cambridge Serial Total Energy Package (CASTEP)⁶¹ engaged in density functional theory (DFT),⁶² incorporating the principle of pseudo-potential plane-wave (PP-PW) total energy calculation to identify the ground state structure of $\text{Cs}_2\text{AgBiI}_6$. To grow electron–ion interactions, the Vanderbilt-type ultrasoft pseudopotential is selected.⁶³ The exchange–correlation potential is enacted through the Generalized Gradient Approximation (GGA) composed with the Perdew–Burke–Ernzerhof (PBE) functional.⁶⁴ For ensuring the convergence the cut-off energy of 520 eV is applied. The Monkhorst–Pack scheme⁶⁵ is employed by taking a k -point mesh of $7 \times 7 \times 7$, which is settled to an ultrafine mode for the first Brillouin zone. However, to see

clearly the electronic charge density pattern, a larger size k -point grid ($12 \times 12 \times 12$) was used. It is also essential to apply the algorithm of Broyden–Fletcher–Goldfarb–Shanno (BFGS) during structural optimization⁶⁶ so that the relatively exact lattice constants and internal atomic coordinates of $\text{Cs}_2\text{AgBiI}_6$ are assessed. It is usual to be relaxed the lattice parameters and atomic positions after structural optimization.⁶⁷ The optimum converging functions to obtain the ground state structure are selected as a maximum force within 0.03 eV, maximum ionic displacement within 0.001 Å, total energy difference within 1×10^{-5} eV per atom, and maximum stress within 0.05 GPa. The electronic and optical properties are then calculated for the optimized structure by considering the aforementioned parameters.

2.2 SCAPS-1D numerical simulation

SCAPS-1D carried out the device modeling and simulation. The continuity, drift-diffusion, and position-dependent Poisson equations provide the backbone of the simulation. The three primary semiconductor equations used in the simulation framework are the continuity equations for holes (eqn (1)), electrons (eqn (2)), and the Poisson equation (eqn (3)), as shown below.^{68,69}

$$\frac{dP_n}{dt} = G_p - \frac{P_n - P_{n0}}{\tau_p} - P_n u_p \frac{dE}{dx} - u_p E \frac{dP_n}{dX} + D_p \frac{d^2 P_n}{dx^2} \quad (1)$$

$$\frac{dn_p}{dt} = G_n - \frac{n_p - n_{p0}}{\tau_n} - n_p u_n \frac{dE}{dx} - u_n E \frac{dn_p}{dX} + D_p \frac{d^2 n_p}{dx^2} \quad (2)$$

$$\begin{aligned} \frac{d}{dX} \left(\varepsilon(x) \frac{d\Phi}{dx} \right) = q[p(x) - n(x) + N_{d^+}(x) - N_{a^-}(x) \\ + p_t(x) - n_t(x)] \end{aligned} \quad (3)$$

where q stands for electron charge, ε stands for dielectric permittivity, G stands for the rate of generation, D stands for the diffusion coefficient, Φ stands for electrostatic potential, E



stands for the electric field, $p(x)$ stands for the number of free holes, $n(x)$ stands for the number of free electrons, $p_t(x)$ stands for the number of trapped holes, $n_t(x)$ stands for the number of trapped electrons, N_d^+ stands for the concentration of donor ionized doping, and N_a^- stands for the concentration of acceptor ionized doping, and x stands for the thickness.

2.3 wxAMPS numerical simulation

The wxAMPS, a program created by the University of Illinois, was used to do a similar numerical analysis as a secondary verification of solar cells' performance in this work.^{70,71} The device behavior is represented *via* resolving Poisson's equation (eqn (4)), which links the electrostatic potential to charge, as well as the electron and hole continuity equations (eqn (5) and (6)) in the different regions of the device structure.

$$\frac{\delta}{\delta x} \left(\epsilon(x) \frac{\delta(\phi(x))}{\delta x} \right) = e\rho \quad (4)$$

$$\frac{1}{e} \frac{\delta J_n}{\delta x} = G(x) - R(x) \quad (5)$$

$$\frac{1}{e} \frac{\delta J_p}{\delta x} = -G(x) + R(x) \quad (6)$$

where x denotes the position, ϵ denotes the dielectric constant, ϕ denotes the local electric potential, e denotes the electron charge, ρ denotes the summed charge density, J_n denotes the electron current density, J_p denotes the hole electron density, G denotes the optical carrier generation rate, and R denotes the overall charge carrier recombination rate. The AMPS-1D program employs two distinct models: the lifetime model and the density of state (DOS) model. For a clear comprehension, the recombination phenomena, and changes in defect states, as well as their effects on the electric field variance across the charges transport materials/perovskite interfaces, were taken into consideration in this study using the density of state model. By resolving three-coupled non-linear differential equations with appropriate boundary conditions, the AMPS-1D can determine the quasi-Fermi level and the electrostatic potential at all locations in the device. The solar cell figures of merit can be computed in accordance with the definitions of these variables based on the device depth.

2.4 Cs₂BiAgI₆-based PSC structure

Here, along with the Cs₂BiAgI₆ absorber layer, ETL, HTL, and back contact are associated to form the structure of double perovskite solar cell. The solar cell structure of the Cs₂BiAgI₆ absorber forms an n-i-p structure. In this instance, an n-i-p structure's superior long-wavelength response makes it preferable to a traditional semiconductor p-n junction, and deep within the device, across the intrinsic area, the depletion zone of an n-i-p structure is present. When a cell is exposed to long wavelength radiation, photons enter the cell deeply. However, only electron-hole pairs produced in and close to the depletion area can contribute to the creation of current. An efficient creation and separation mechanisms of electron-hole pairs are made possible by the greater depletion width, which raises the

Table 1 Input optimization parameters of the TCO, ETL, and absorber layer of the study

Parameters	ITO	TiO ₂	PCBM	ZnO	C ₆₀	IGZO	SnO ₂	WS ₂	CeO ₂	Cs ₂ BiAgI ₆
Thickness (nm)	500	30	50	50	50	30	100	100	100	800 ^a
Band gap, E_g (eV)	3.5	3.2	2	3.3	1.7	3.05	3.6	1.8	3.5	1.6
Electron affinity, X (eV)	4	4	3.9	4	3.9	4.16	4	3.95	4.6	3.90
Dielectric permittivity (relative), ϵ_r	9	9	3.9	9	4.2	10	9	13.6	9	6.5
CB effective density of states, N_C (1/cm ³)	2.2×10^{18}	2×10^{18}	2.5×10^{21}	3.7×10^{18}	8.0×10^{19}	5×10^{18}	2.2×10^{18}	1×10^{18}	1×10^{20}	1×10^{19}
VB effective density of states, N_V (1/cm ³)	1.8×10^{19}	1.8×10^{19}	2.5×10^{21}	1.8×10^{19}	8.0×10^{19}	5×10^{18}	1.8×10^{19}	2.4×10^{19}	2×10^{21}	1×10^{19}
Electron mobility, μ_n (cm ² V ⁻¹ s ⁻¹)	20	20	0.2	100	8.0×10^{-2}	15	100	100	100	2
Hole mobility, μ_h (cm ² V ⁻¹ s ⁻¹)	10	10	0.2	25	3.5×10^{-3}	0.1	25	100	25	2
Shallow uniform acceptor density, N_A (1/cm ³)	0	0	0	0	0	0	0	0	0	1×10^{15a}
Shallow uniform donor density, N_D (1/cm ³)	1×10^{21}	9×10^{16}	2.93×10^{17}	1×10^{18}	1×10^{17}	1×10^{17}	1×10^{18}	1×10^{21}	10^{21}	0 ^a
Defect density, N_t (1/cm ³)	1×10^{15a}	1×10^{15a}	1×10^{15a}	1×10^{15a}	1×10^{15a}	1×10^{15a}	1×10^{15a}	1×10^{15a}	1×10^{15a}	1×10^{15a}
Reference	14	14	14	14	14	14	14	14	14	72

^aThis study.



Table 2 Input optimization parameters HTL the study¹⁴

HTL	Cu ₂ O	CuSCN	Cu ₂ SnS ₂	P3HT	PEDOT:PSS	Spiro-MeOTAD	NiO	CuI	CuO	V ₂ O ₅	CFTS	CBTS
Thickness (nm)	50	50	50	50	200	100	100	50	100	100	100	100
Band gap, E_g (eV)	2.2	3.6	1.58	1.7	1.6	3	3.8	3.1	1.51	2.20	1.3	1.9
Electron affinity, X (eV)	3.4	1.7	4.2	3.5	3.4	2.2	1.46	2.1	4.07	4.00	3.3	3.6
Dielectric permittivity (relative), ϵ_r	7.5	10	14.6	3	3	10.7	6.5	18.1	10.00	9	5.4	5.4
CB effective density of states, N_C (1/cm ³)	2×10^{19}	2.2×10^{19}	2×10^{18}	2×10^{21}	2.2×10^{18}	2.2×10^{18}	2.8×10^{19}	2.8×10^{19}	2.2×10^{19}	9.2×10^{17}	2.2×10^{18}	2.2×10^{18}
VB effective density of states, N_V (1/cm ³)	1×10^{19}	1.8×10^{18}	1×10^1	2×10^{21}	1.8×10^{19}	1.8×10^{19}	1×10^{19}	1×10^{19}	5.5×10^{20}	5.0×10^{18}	1.8×10^{19}	1.8×10^{19}
Electron mobility, μ_n (cm ² V ⁻¹ s ⁻¹)	200	100	49	1.8×10^{-3}	4.5×10^{-2}	2.1×10^{-3}	12	100	100	3.2×10^2	21.98	30
Hole mobility, μ_h (cm ² V ⁻¹ s ⁻¹)	8600	25	49	1.86×10^{-2}	4.5×10^{-2}	2.16×10^{-3}	2.8	43.9	0.1	4.0×10^1	21.98	10
Shallow uniform acceptor density, N_A (1/cm ³)	1×10^{18}	1×10^{18}	1×10^{18}	1×10^{18}	1.0×10^{18}	1×10^{18}	1.0×10^{18}	1×10^{18}	1×10^{18}	1×10^{18}	1×10^{18}	1×10^{18}
Shallow uniform donor density, N_D (1/cm ³)	0	0	0	0	0	0	0	0	0	0	0	0
Defect density, N_t (1/cm ³)	1.0×10^{15a}	1×10^{15a}	1×10^{15a}	1×10^{15a}	1×10^{15a}	1×10^{15a}	1×10^{15a}	1×10^{15a}	1×10^{15a}	1×10^{15a}	1×10^{15a}	1×10^{15a}

^a This study.

cell's quantum efficiency.¹⁴ $\text{Cs}_2\text{BiAgI}_6$ captures photons due to double heterostructure it ensures the charge and photon confinement and both sides of highly doped ETL and HTL work as an ohmic contact. During the study SCAPS-1D, the software helps us to investigate the performance of various structures of double PSCs. By keeping the ambient temperature 300 K, frequency 1 MHz, and AM 1.5 G sunlight spectrum double perovskite structures are formed. Also taken eight ETLs and twelve HTLs, back contact as Au to investigate the different structures and their optoelectronic parameters are set up initially from the different studies which are mentioned in Tables 1–3.

3 Results and discussion

3.1 Analysis of DFT results

3.1.1 Structural properties of $\text{Cs}_2\text{BiAgI}_6$ compound.

According to the optimization output, the crystal structure of $\text{Cs}_2\text{AgBiI}_6$ is a cubic double-perovskite-type system with space group $Fm\bar{3}m$ (#225). The atomic positions of Cs, Ag, Bi, and I in the unit cell are 8c (0.25, 0.25, 0.25), 4a (0, 0, 0), 4b (0.5, 0.5, 0.5), and 24e (0.2513, 0, 0). The optimized three-dimensional crystal structure of $\text{Cs}_2\text{AgBiI}_6$ is projected in Fig. 1(b). The calculated lattice parameter $a = 8.6338 \text{ \AA}$ is lower than that of the previously reported lattice parameter of similar double perovskite-type compound $\text{Cs}_2\text{AgBiBr}_6$ ($a = 11.430 \text{ \AA}$)⁵⁹ due to the difference of atomic radius between I and Br as well as using different calculation parameters. However, the negative value of formation energy ($\Delta E_f = -2.66 \text{ eV}$ per atom) calculated by the following equation (eqn (7)) confirms the thermodynamic stability of optimized $\text{Cs}_2\text{AgBiI}_6$.⁷³

$$\Delta E_f(\text{Cs}_2\text{AgBiI}_6) =$$

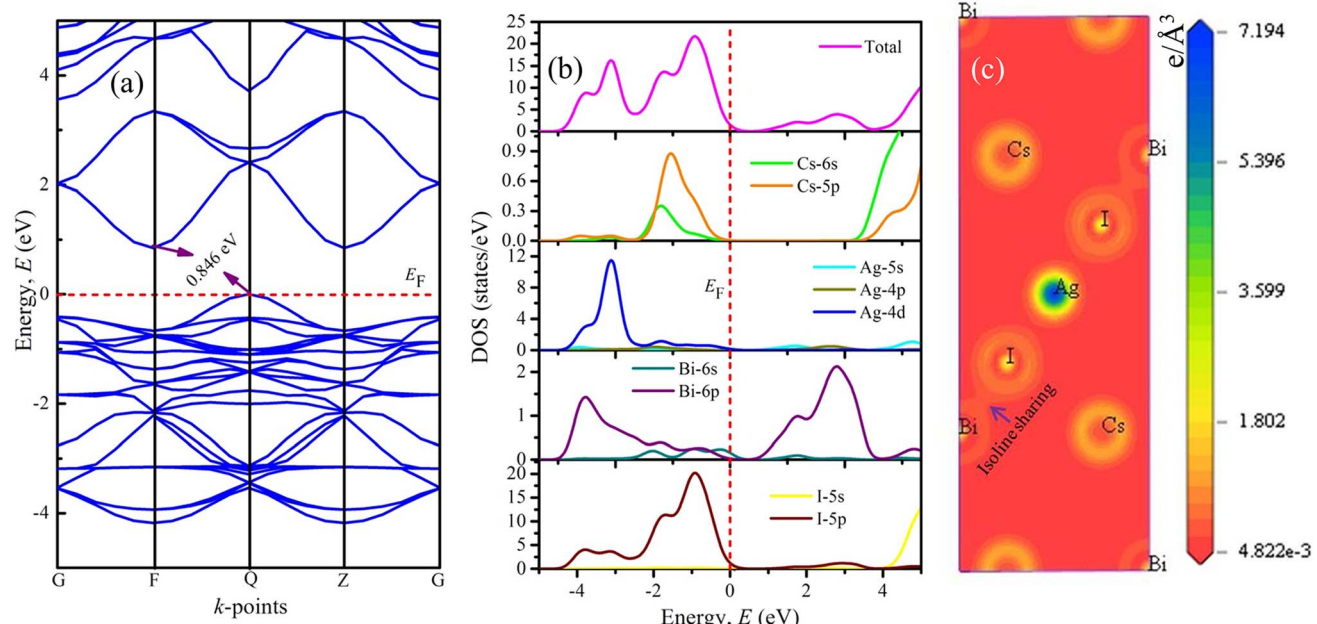
$$\frac{[E_{\text{tot}}(\text{Cs}_2\text{AgBiI}_6) - 2E_s(\text{Cs}) - E_s(\text{Ag}) - E_s(\text{Bi}) - 6E_s(\text{I})]}{N} \quad (7)$$

Here, $E_s(\text{Cs})$, $E_s(\text{Ag})$, $E_s(\text{Bi})$, and $E_s(\text{I})$ are the energy of Cs, Ag, Bi, and I atoms, respectively, while $E_{\text{tot}}(\text{Cs}_2\text{AgBiI}_6)$ is the unit cell total energy of $\text{Cs}_2\text{AgBiI}_6$, and N represents the number of atoms in the unit cell.

3.1.2 Band structure and DOS of $\text{Cs}_2\text{BiAgI}_6$ compound. The electronic properties provide important information to explain materials' bonding nature, photon-absorbing behaviours, and other relevant properties.⁷⁴ A compound's electronic properties are mostly related to its band structure, the density of states (DOS), and charge density. The result of band structure calculation along the highly symmetric directions within the k -space for $\text{Cs}_2\text{AgBiI}_6$ is presented in Fig. 2(a), where a red horizontal dash line at 0 eV indicates the Fermi level (E_F). The bands below and above the E_F are usually called the valence and conduction bands, respectively. It is observed from Fig. 2(a) that either the valence or conduction band is not crossed the E_F and overlaps with each other. Hence the compound $\text{Cs}_2\text{AgBiI}_6$ has a band gap in its electronic band structure. The calculated band gap is found to be 0.846 eV. The band gap value of the studied compound is somewhat lower than that of other similar double perovskite-type compounds $\text{Cs}_2\text{AgBiBr}_6$ (2.19 eV),²⁶ $\text{Cs}_2\text{AgBiCl}_6$ (2.77 eV),²⁶ $\text{Cs}_2\text{AgInCl}_6$ (3.23 eV),⁷⁵ and $\text{Cs}_2\text{AgSbCl}_6$ (1.40 eV).⁶⁰

Table 3 Input parameters of interface defect layers¹⁴

Interface	Defect type	Capture cross section: electrons/holes (cm ²)	Energetic distribution	Reference for defect energy level	Total density (cm ⁻³) (integrated over all energies)
ETL/Cs ₂ BiAgI ₆	Neutral	1.0 × 10 ⁻¹⁷ 1.0 × 10 ⁻¹⁸	Single	Above the VB maximum	1.0 × 10 ¹⁰
	Neutral	1.0 × 10 ⁻¹⁸ 1.0 × 10 ⁻¹⁹			1.0 × 10 ¹⁰
Cs ₂ BiAgI ₆ /HTL	Neutral	1.0 × 10 ⁻¹⁸ 1.0 × 10 ⁻¹⁹	Single	Above the VB maximum	1.0 × 10 ¹⁰
	Neutral	1.0 × 10 ⁻¹⁹			1.0 × 10 ¹⁰

Fig. 2 (a) Calculated band structure of Cs₂AgBiI₆ along the high-symmetry direction, (b) calculated total and partial density of states of Cs₂AgBiI₆, and (c) the charge density mapping of Cs₂AgBiI₆ along (111) crystallographic plane.

Moreover, the minimum conduction band and maximum valence band are observed at F- and Q-points, respectively, exhibiting the indirect semiconducting nature of double perovskite compound Cs₂AgBiI₆. Besides, the valence band maximum is the nearest band to the E_F , which ensures the p-type semiconducting nature of chosen double perovskite. Interestingly, some nearly flat valence bands between F- and Z-points close to the E_F are also observed. This highly dispersive nature of the bands near the E_F indicated the high mobility of charge carriers and predicted that the effective mass would be significantly higher in these bands.

Fig. 2(b) represents the total density of state (TDOS) together with the partial density of state (PDOS), which are used to understand further the contributions of different atoms/orbitals and the chemical bonding nature in Cs₂AgBiI₆. In the DOS diagram, the E_F is represented by the red vertical dashed line fitted at 0 eV. The TDOS diagram confirms the band gap in the electronic structure of the studied double perovskite, reflecting a similar nature as the band diagram. The valence band mainly consists of Ag-4d and I-5p states together with the minimal contributions of Cs-6s, Cs-5p, and Bi-6p orbitals. On the other hand, the conduction band in the vicinity of the E_F

mostly arises from the Bi-6p state. However, the conduction band over 4 eV originated from the significant contribution of I-5s with a small share of 6s and 5p states of the Cs atom. Notably, the valence band maximum at the Q-point of the Brillouin zone near the E_F is generated due to the influence of the I-5p state. As a result, in the PDOS of the investigated compound, the orbital electrons of the I-5s/5p orbitals are crucial for absorbing light energy and producing conductivity.

3.1.3 Electron charge density of Cs₂BiAgI₆ compound. To understand and give a clear explanation of the charge transformation and nature of bonding among constituent atoms of double perovskite Cs₂AgBiI₆, the study of charge density mapping is crucial.^{54,55} The charge density mapping along the (111) crystallographic plane is illustrated in Fig. 2(c), in which the right scale shows the intensity of electron density (blue and red colors denote the highest and lowest intensity of electron density, respectively). The highest intensity of charge density is observed around the Ag atom, whereas it is lowest around the Bi atom. The charge contours of the Cs and I atoms do not overlap, indicating the existence of ionic bonding between these two atoms. A similar phenomenon is also noticed for Ag and I atoms, revealing the ionic nature of Ag-I bonds. On the other



hand, the elliptical contour of charges between Bi and I atoms exhibits the presence of strong covalent bonding of Bi–I bonds. Moreover, isoline sharing suggests that a charge transfer between these two atoms may occur. The strong covalent nature of Bi–I bonds mainly originated from the hybridization between the electronic orbital states of Bi-6p and I-5p.

3.1.4 Optical properties of $\text{Cs}_2\text{BiAgI}_6$ compound. The optical functions are essential for understanding the behavior of a material when an incident electromagnetic wave interacts with it. Therefore, these functions bear crucial significance for exploring possible uses of material in photovoltaic and optoelectronic instruments. In such cases, the nature of a specific material under incident photon (infrared, visible, and ultraviolet) is necessary to examine. A number of optical processes, namely, dielectric constant $\varepsilon(\omega)$, refractive index $n(\omega)$, absorption $\alpha(\omega)$, conductivity $\sigma(\omega)$, and reflectivity $R(\omega)$ are determined to investigate the response of $\text{Cs}_2\text{AgBiI}_6$ upon photon energies up to 30 eV. Generally, both the intra-band and inter-band transitions are used to calculate the $\varepsilon(\omega)$. However, the present calculation overlooks the intra-band contributions that are arisen from indirect transitions. This is because of the inclusion of phonon in the indirect intra-band transition and possesses a limited scattering cross-section⁷⁶ related to the direct transition. Hence, there is no need to retain the momentum of phonon scattering. It can be seen from Fig. 3(a) that the real and imaginary parts of the dielectric function are higher at low energy and remarkably reduced in high-energy regions. This matter hints at the useful usage of $\text{Cs}_2\text{AgBiI}_6$ in microelectronic devices and integrated circuits.¹⁴ The $\varepsilon(\omega)$ is connected to electron excitement that originates predominantly

because of interband transitions and exhibits minor peaks at ~ 6 eV due to intraband transitions. The real and imaginary parts of $n(\omega)$ are shown in Fig. 3(b). The real part falls gradually in a similar fashion as the real part of the dielectric function, whereas the imaginary part slightly exceeds the real part at ~ 9 eV and then again falls below the real part at ~ 16 eV. The real part of the refractive index is relatively large at zero photon energy, and the maximum is found at ~ 2 eV. It suggests the possible device applications of a chosen compound in quantum-dot light-emitting diodes, organic light-emitting diodes, solar cells, and waveguides.^{54,73}

The $\alpha(\omega)$ presented in Fig. 3(c) manifests the spectra around 0–26 eV owing to the transitions between energy bands. Importantly, it starts from slightly above zero energy, which reconfirms the small band gap of $\text{Cs}_2\text{AgBiI}_6$. The $\alpha(\omega)$ is relatively higher at lower photon energy, which predicts the studied compound's potential use in solar panels. Due to the semi-conducting nature of $\text{Cs}_2\text{AgBiI}_6$, the $\sigma(\omega)$ also does not start at zero energy (Fig. 3(d)). It starts at ~ 0.84 eV, and the maximum spectrum is attained at 6 eV, which becomes lower with increasing energy. The large conductivity at lower photon energy suggests the conventional applications of $\text{Cs}_2\text{AgBiI}_6$. It can be noticed from Fig. 3(e) that the static reflectivity $R(0)$ is $\sim 21\%$ of total radiation, which is increased in the high-energy region because of inter-band transitions. Moreover, the $R(\omega)$ exhibits lower values ($<44\%$) over the studied energy range, indicating significant absorptivity/transmissivity of light, which means that this compound may absorb a significant number of photons and making it suitable for use in optoelectronic devices.⁵⁴

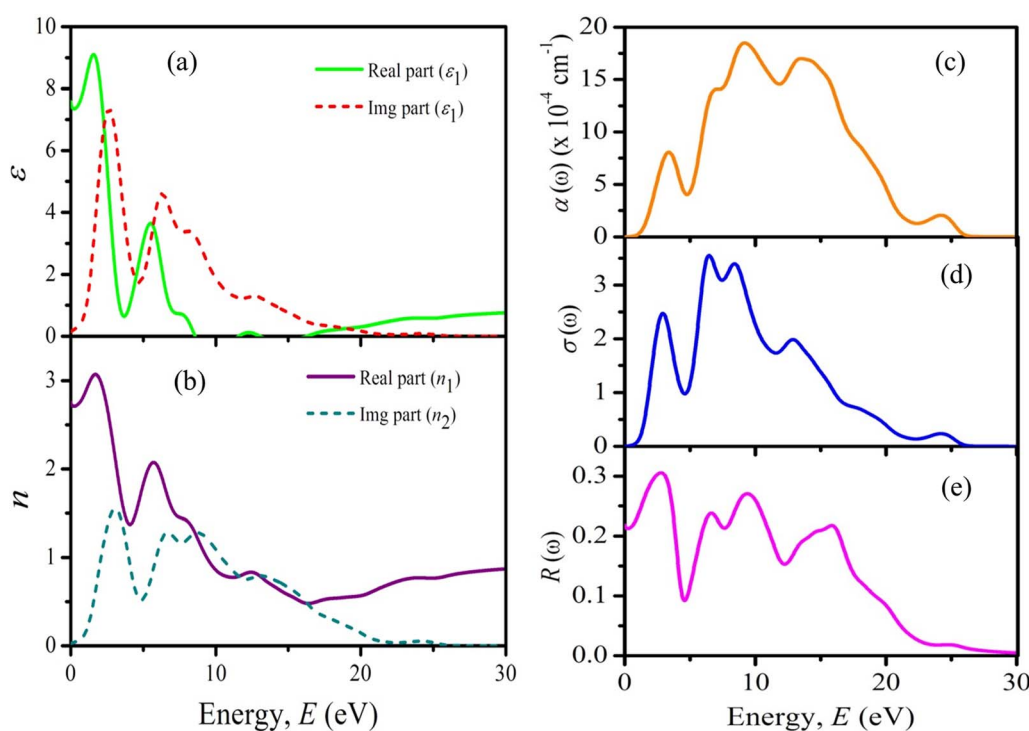


Fig. 3 Calculated (a) dielectric function, (b) refractive index, (c) absorption, (d) conductivity, and (e) reflectivity of $\text{Cs}_2\text{AgBiI}_6$.



3.2 Analysis of SCAPS-1D results

3.2.1 Effect of HTL layer. In the PSCs device configuration, HTL collects holes from the perovskite ($\text{Cs}_2\text{BiAgI}_6$) and then transfers them to the back metal contact (Au). Twelve types of HTL have been utilized in SCAPS-1D simulation to optimize the device's performance (Table 2). The visual depiction of the HTL optimization process is shown in Fig. 4. Fig. 4(a) illustrates that PCBM as ETL is optimized with CBTS as HTL compared to the other HTL, while the PCE of this perovskite device configuration is 19.99%. Besides, TiO_2 as ETL showed maximum optimization with CBTS as HTL in Fig. 4(b), with a PCE of 21.55%. Fig. 4(c) demonstrates that ZnO as ETL with CBTS as HTL exhibited more optimization than other HTL, with a PCE of 21.59%. Similarly, SnO_2 , IGZO, and WS_2 as ETL with CBTS as HTL demonstrated the highest optimization compared to other

HTLs. The PCEs of these device configurations are 21.52%, 20.42%, and 21.43% respectively (Fig. 4(d), (e), and (f)). And the C_{60} and CeO_2 as ETL with CBTS as HTL showed the best optimization than other HTLs, with PCE of 17.47% and 14.44%, respectively. Compared to the other HTL presented in this study, CBTS exhibited the highest performance with different ETL. Therefore, CBTS is suitable for HTL optimization among numerous simulated device configurations.

3.2.2 ETL optimization. In the PSCs device configuration, ETL removes the electron from the perovskite materials and then transfers the electron to the ITO. ETL also prevent electron in ITO from recombining with the absorber layer's holes.⁷⁷ Simulating each ETL with different HTL in the $\text{Cs}_2\text{BiAgI}_6$ perovskite absorber optimizes the performance of device configuration (Tables 1 and 2). In this study, we used electron transport materials (ETMs) such as TiO_2 , PCBM, ZnO , C_{60} ,

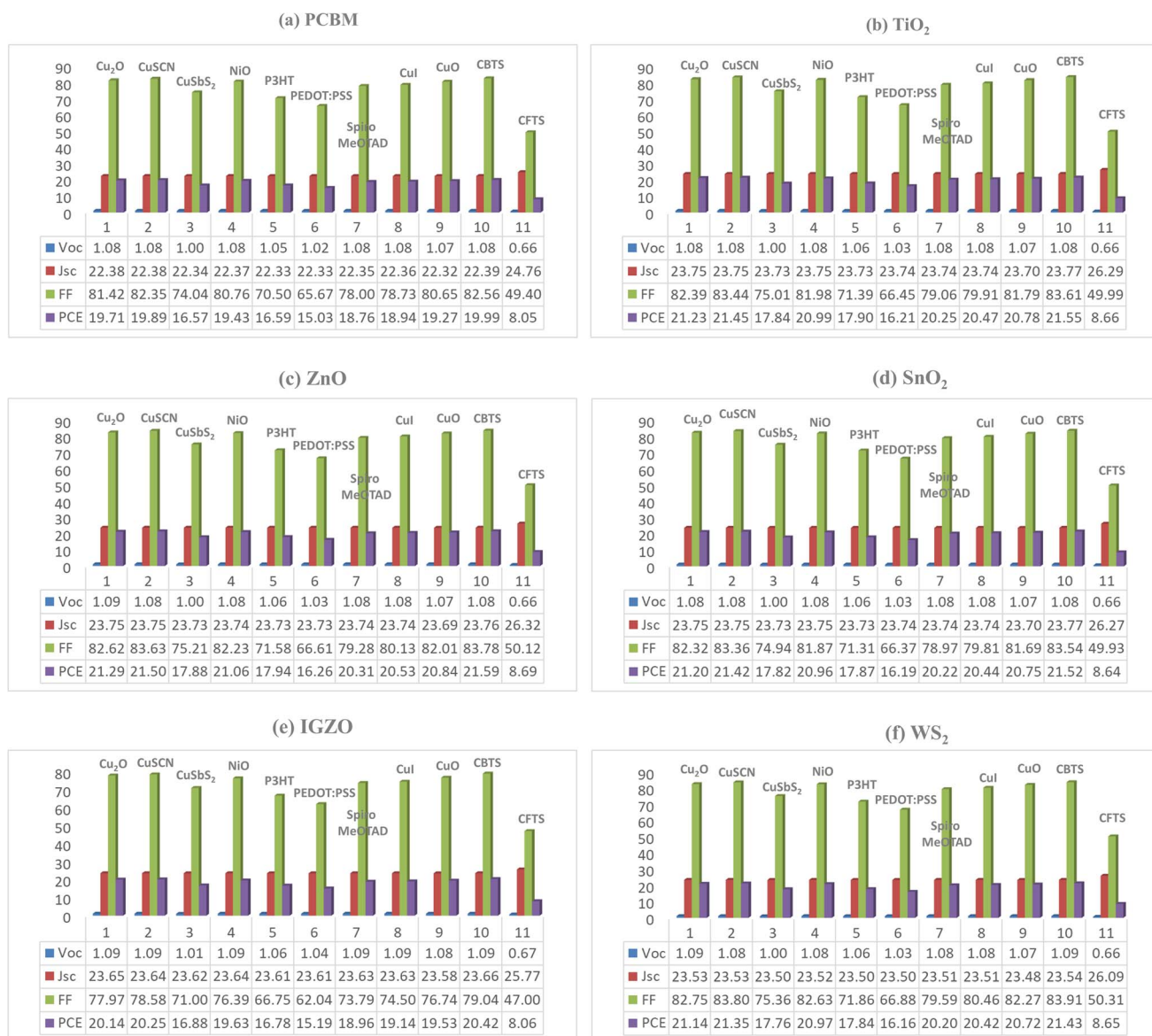


Fig. 4 Variation of performance parameters, i.e., V_{OC} (V), J_{sc} (mA cm^{-2}), FF (%), and PCE (%) of $\text{Cs}_2\text{BiAgI}_6$ absorber layer-based PSCs device for different HTLs with Au as back metal contact and ETLs of (a) PCBM, (b) TiO_2 , (c) ZnO , (d) SnO_2 , (e) IGZO, and (f) WS_2 .



IGZO, SnO₂, WS₂, and CeO₂ with different electron transport materials (HTMs). After simulating all possible combinations between the ETM layer and HTM layer with Cs₂BiAgI₆ absorber

and Au metal contact, all ETL showed maximum optimization with CBTS as HTL. As a result, eight sets of device configurations from ninety-six combinations exhibited maximum

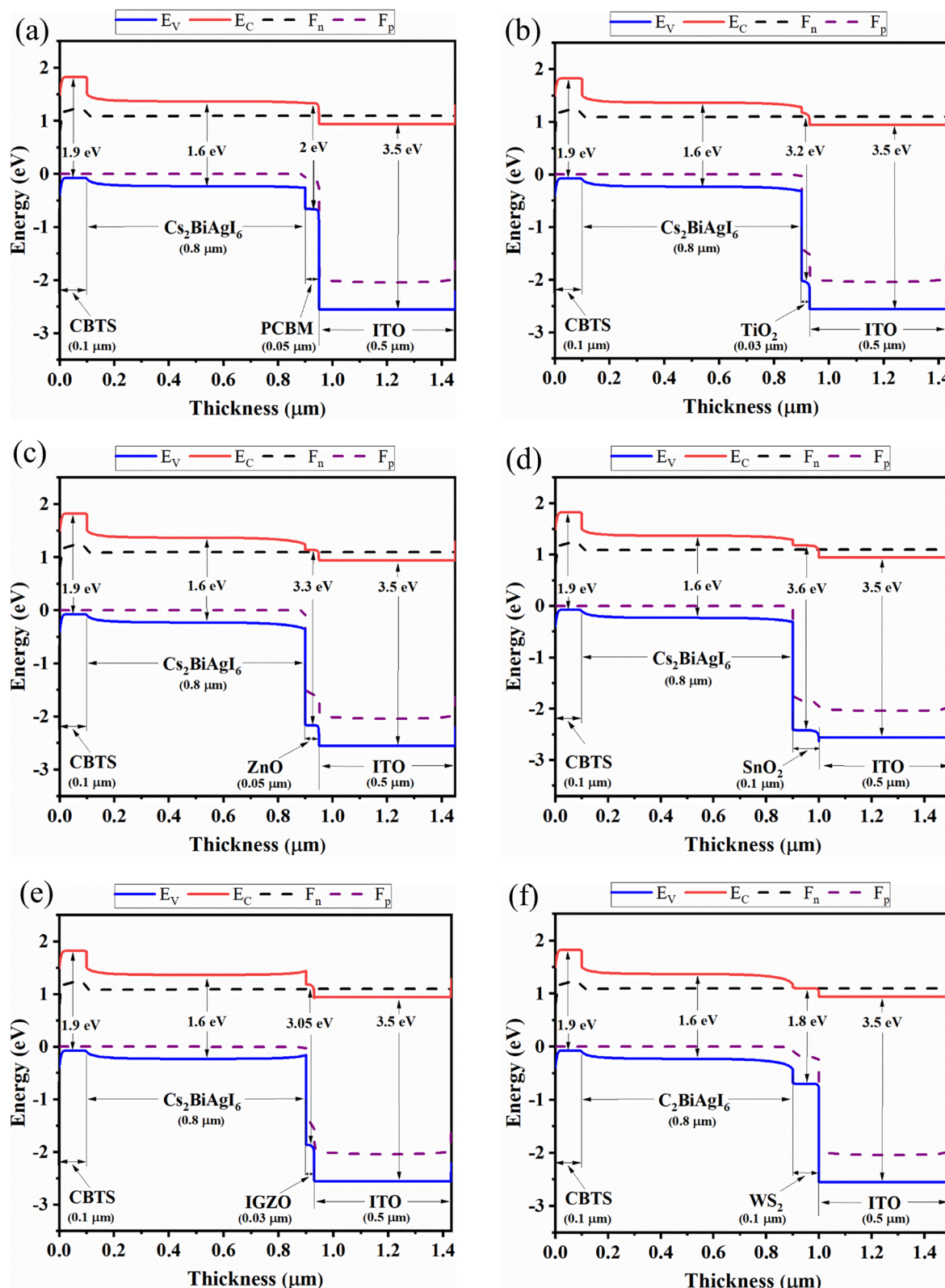


Fig. 5 Energy band diagram of solar cells structure with different ETMs of (a) PCBM, (b) TiO₂, (c) ZnO, (d) SnO₂, (e) IGZO, and (f) WS₂.

Table 4 Optimized performance parameters of the best combination for each of the ETLs and HTLs

Optimized device	Cell thickness (μm)	V _{OC} (V)	J _{SC} (mA cm ⁻²)	FF (%)	PCE (%)
ITO/PCBM/Cs ₂ BiAgI ₆ /CBTS/Au	0.5/0.05/0.8/0.1/Au	1.081	22.39	82.56	19.99
ITO/TiO ₂ /Cs ₂ BiAgI ₆ /CBTS/Au	0.5/0.03/0.8/0.1/Au	1.084	23.80	83.61	21.55
ITO/ZnO/Cs ₂ BiAgI ₆ /CBTS/Au	0.5/0.05/0.8/0.1/Au	1.085	23.76	83.78	21.59
ITO/C ₆₀ /Cs ₂ BiAgI ₆ /CBTS/Au	0.5/0.05/0.8/0.1/Au	1.077	19.62	82.65	17.47
ITO/IGZO/Cs ₂ BiAgI ₆ /CBTS/Au	0.5/0.03/0.8/0.1/Au	1.092	23.66	79.04	20.42
ITO/SnO ₂ /Cs ₂ BiAgI ₆ /CBTS/Au	0.5/0.1/0.8/0.1/Au	1.084	23.77	83.54	21.52
ITO/CeO ₂ /Cs ₂ BiAgI ₆ /CBTS/Au	0.5/0.1/0.8/0.1/Au	0.924	23.59	66.21	14.44
ITO/WS ₂ /Cs ₂ BiAgI ₆ /CBTS/Au	0.5/0.1/0.8/0.1/Au	1.085	23.54	83.91	21.43

optimized performance and efficiency of device configurations. While band alignment of ZnO (3.3 eV), TiO₂ (3.2 eV), and SnO₂ (3.6 eV) ETL was significantly higher in comparison with other ETLs which showed $\geq 21.5\%$ efficiency with CBTS HTL (Fig. 5). On the contrary, CeO₂ (3.5 eV) band alignment isn't convenient with the Cs₂BiAgI₆ absorber and CBTS HTL which performed an efficiency of 14.44%. Table 4 illustrates the performance parameters V_{OC} , J_{SC} , FF, and PCE, which exhibited good agreement value in these eight device configurations.

3.2.3 Band diagram. The energy band diagram utilizes each ETL with a Cs₂BiAgI₆ absorbing layer and CBTS as HTL influencing valence/conduction band offset (*i.e.*, valence band difference between HTL and the absorber layer and conduction band between ETL and absorber layer). The alignment of the energy levels has a significant impact on the efficiency and performance of the PSCs. In the PSCs, photo-generated electrons are injected into the ETL conduction band, and at the same time, holes are transported to the HTL. Afterward, electrons and holes are collected at their respective front (ITO) and back contact metal (Au) correspondingly. The energy band mismatch at the ETL/Cs₂BiAgI₆ and the Cs₂BiAgI₆/HTL interface significantly impacts the device's performance parameters. The nature of the interface controls the effect of interfacial recombination. Therefore, carefully tuning the electronic properties of ETL and HTL materials became a vital task. Thus, the electron affinity of ETL should be higher than that of Cs₂BiAgI₆ to extract the electron safely at the ETL/Cs₂BiAgI₆ interface, and the ionization energy of HTL should be lower than that of Cs₂BiAgI₆ to extract the holes at the Cs₂BiAgI₆/HTL interface. Fig. 5 shows that the Fermi level, which is near the conduction band, enters into the conduction band in the case of the best eight sets of Cs₂BiAgI₆-based device configuration. The PCBM as ETM layer and CBTS as HTM layer associated with Cs₂BiAgI₆-based device configuration showed that the Fermi level crossed the conduction band, as shown in Fig. 5(a). Fig. 5(c)–(h) exhibited the others of Cs₂BiAgI₆-based perovskite device configurations where TiO₂, ZnO, C₆₀, IGZO, SnO₂, WS₂, and CeO₂ as ETL and CBTS as HTL showed the same pattern and degenerate semiconductors nature as like Fig. 5(a).

3.2.4 Effect of absorber and ETL thickness on cell performance. The effect of the absorber layers and different ETL layer thicknesses of desired eight double perovskites solar cell structures are investigated through contour plot mapping to evaluate the solar cell's performance parameters. An appropriate absorber and ETL selection of any solar cell is the primary

and crucial element in achieving high-performance solar cells. Moreover, the appropriate thickness of the absorber and ETL helps to capture the light and collect holes from the absorber layer, accordingly. Fig. 6 represents the effect of ETL and absorber layer thickness on the V_{OC} parameter of the eight most efficient solar cell structures enlisted in Table 4. From Fig. 6(a), it is observed that ETL thickness is 0.1 μm and absorber thickness is in the range of 0.4 μm in the case of ETL as a PCBM-associated structure. In addition, simultaneously increasing ETL thickness with absorber layer thickness can cause lower V_{OC} (Fig. 6(a)). For the TiO₂ and ZnO as ETL-associated structures, the thickness of the absorber layer remains constant with increasing ETL layer thickness (Fig. 6(b) and (c)). The highest value of V_{OC} for TiO₂ and ZnO as ETL-associated structures are exhibited at around 0.3 μm and 0.5 μm absorbers layer thickness regardless of ETL thickness (Fig. 6(b) and (c)). For the C₆₀ as ETL associated structure, the highest V_{OC} is exhibited when absorber thickness is around 0.4 μm, and ETL thickness is about 0.1 μm (Fig. 6(d)). On the other hand, for IGZO as ETL, the higher V_{OC} value is shown when the absorber layer is <0.4 μm with regardless of the ETL layer thickness (Fig. 6(e)). The SnO₂ as ETL-associated solar cell structure shows V_{OC} at a similar range at a particular absorber layer thickness, which is 0.5 to 0.6 μm (Fig. 6(f)). The V_{OC} values of CeO₂ as an ETL-associated solar cell structure are shown between 0.1 to 0.2 μm ETL thickness and 0.4 to 0.5 μm absorber layer thickness (Fig. 6(g)). According to Fig. 6(h), WS₂ as an ETL-associated solar structure shows a higher V_{OC} at around 0.03 to 0.25 μm of ETL thickness and 0.3 to 0.4 μm absorber thickness. In conclusion, the larger thickness of the absorber layer might be the cause of lower V_{OC} for most of the studied solar structures, as observed in Fig. 6. This fact is explained by the increase in carrier recombination rate in the presence of a thick absorber layer, causing a rise in saturation current larger than photocurrent.

Fig. 7 represents the effect of variation of ETL and absorber layer thickness on the J_{SC} parameter of eight desired perovskite solar cells. For PCBM as an ETL-associated solar cell, the maximum J_{SC} (22.08 to 24 mA cm⁻²) value is exhibited when the ETL thickness is 0.03 to 0.1 μm and the absorber thickness is 0.6 to 1.3 μm (Fig. 7(a)). The almost similar pattern we have observed for ETL C₆₀ – associated solar cells, where the higher J_{SC} (19.74 to 22.10 mA cm⁻²) value is observed when absorber thicknesses are from 0.6 to 1.3 μm and ETL thicknesses are from ≤ 0.1 μm (Fig. 7(d)). It is observed that the lower ETL thickness and higher absorber thickness can cause higher J_{SC} .



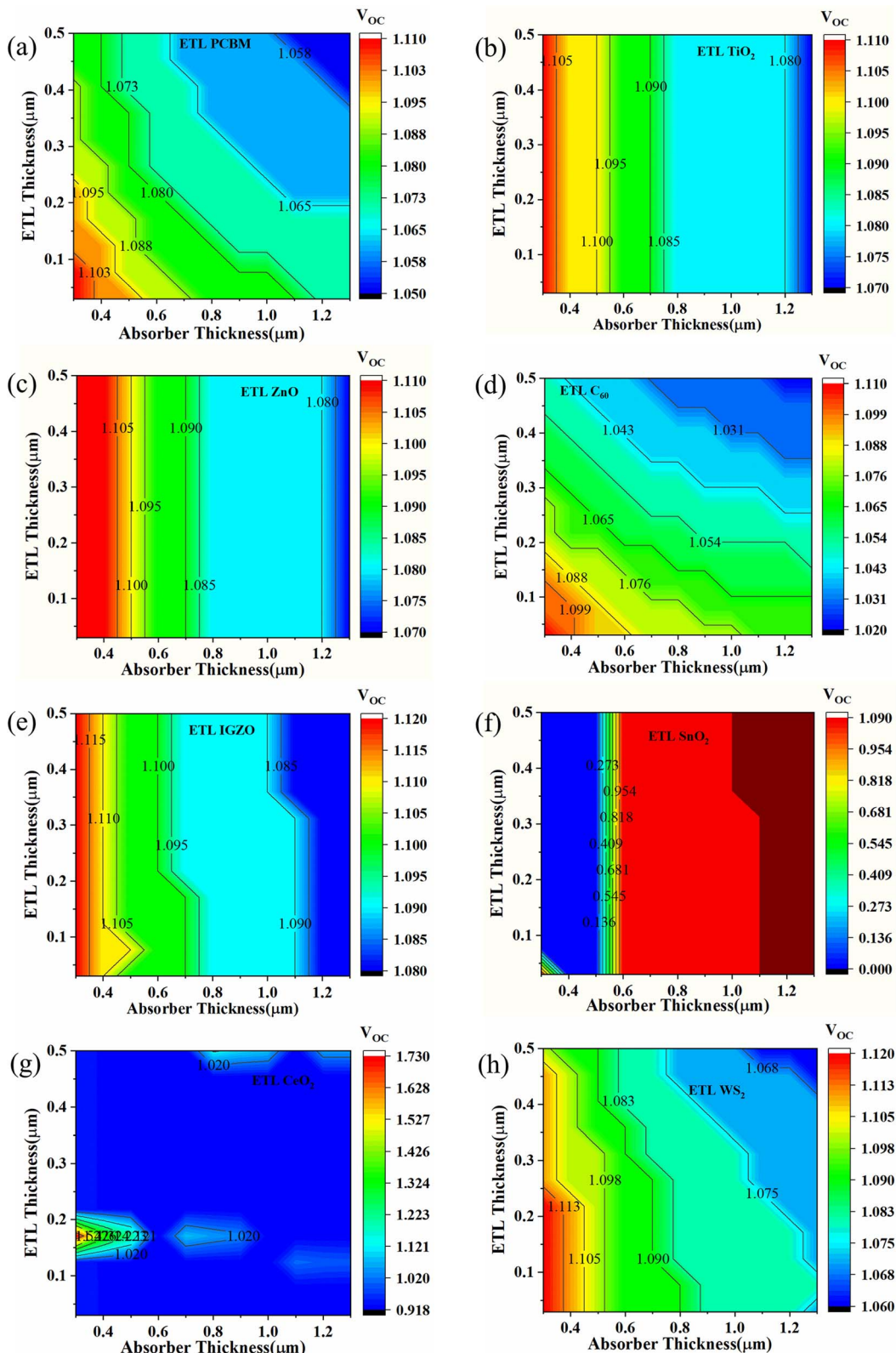


Fig. 6 Contour mapping of V_{OC} (V) when ETL as (a) PCBM, (b) TiO_2 , (c) ZnO , (d) C_{60} , (e) IGZO, (f) SnO_2 , (g) CeO_2 , and (h) WS_2 .

Higher absorber thickness permits more light collection and hence increases the generation rate, giving a high J_{SC} value. Thin ETL can boost the current *via* decreasing electron–hole

pair recombination which reduces the effect of series resistance. Besides, minimizing the ETL thickness prevents the formation of wider pinholes and rough terrain surfaces, which



can severely impede the J_{SC} , V_{OC} , and therefore efficiency. The maximum J_{SC} value for TiO_2 as ETL and ZnO as ETL-associated solar structures are shown to be the same when the absorber layer thicknesses are 0.8 to 1.3 μm , and ETL thickness doesn't make any significant effect during the variation (Fig. 7(b) and (c)). From Fig. 7(e), we observe that IGZO as ETL associated solar cell structure shows a maximum J_{SC} pattern, which is almost 24 $mA\ cm^{-2}$ when absorber thickness is 0.8 to 1.3 μm , and ETL thickness is 0.03 to 0.3 μm . The SnO_2 as an ETL-associated solar structure shows a moderate J_{SC} pattern range with the absorber and ETL thickness variation (Fig. 7(f)). In the case of CeO_2 as ETL, the maximum J_{SC} is 23.58 to 24.20 $mA\ cm^{-2}$ when absorber thickness is about 0.8 to 1.3 μm , regardless of ETL thickness (Fig. 7(g)). Finally, WS_2 as an ETL-associated solar cell shows the highest J_{SC} ($24.50\ mA\ cm^{-2}$) pattern when absorber thickness is 0.7 to 1.3 μm and ETL thickness is 0.03 to 0.2 μm (Fig. 7(g)).

The effect on FF values for the variation of absorber and ETL layer thickness is shown in Fig. 8. For PCBM as an ETL-associated solar structure, it is observed that FF values are decreased with increased absorber and ETL layer thickness (Fig. 8(a)). This fact is due to the increased series resistance. The lowest FF is observed at around 79.16%, as shown in Fig. 8(a). A similar pattern is observed for TiO_2 , ZnO , C_{60} , IGZO, and WS_2 -associated solar structures (Fig. 8(b)–(e), and (h)). However, Fig. 8(f) shows that when SnO_2 is an ETL, the FF values are observed from 31 to 50%. In contrast, the FF values for CeO_2 as ETL-associated solar cells are increased with decreased absorber thickness (Fig. 8(g)). An anomaly of the FF pattern is observed for different ETL layer thicknesses (around 0.03–0.5 μm) with different absorber layers (Fig. 8(g)).

Fig. 9(a) and (d) show that PCBM and C_{60} , as ETL-associated solar cells exhibit the same pattern with increasing absorber and ETL layer thickness. The highest PCE of PCBM and C_{60} as ETL is 20.90% and 19.30% when the ETL thickness is less than 0.7 μm and the absorber layer thickness is 0.4 to 1.3 μm . The TiO_2 and ZnO as ETL-associated solar cells show the same pattern for PCE with increasing ETL and absorber layer thickness (Fig. 9(b) and (c)). The highest PCE is observed when the absorber layer thickness is more than 0.6 μm regardless of ETL thickness, as shown in Fig. 9(b) and (c). For IGZO as ETL, the maximum PCE (20.40%) is observed when the absorber layer thickness is 0.5 to 1.1 μm and the ETL layer thickness is 0.03 to 0.1 μm (Fig. 9(e)). The PCE pattern is almost moderate in the case of SnO_2 as an ETL-associated solar structure (Fig. 9(f)). For CeO_2 as ETL, the highest PCE is observed when absorber thickness is 0.5 to 0.7 μm , and ETL thickness does not significantly impact the PCE pattern, as shown in Fig. 9(g). Finally, in the range of 0.5 to 1.5 μm absorber and less than 0.15 μm ETL thickness, the PCE is highest for WS_2 as an ETL-associated solar structure (Fig. 9(h)).

The changing trend of V_{OC} , J_{SC} , FF, and PCE of perovskite solar cells with different ETL is very distinct due to several reasons. The absorption coefficient significantly affects the PV parameters like V_{OC} , J_{SC} , FF, and PCE and is directly linked with the bandgap of the ETLs. It also affects the coupling of incident photons in the underlying Cs_2BiAgI_6 absorber layer. The conduction band offset (CBO) which depends on the work function (affinity + fermi energy level) difference between ETL

and absorber layer may also play a crucial role in the performance of the solar cell. Where there is a preferred electron affinity, it can have a big impact on how well the solar cell works. Energy cliffs with CBO (–) and energy spikes with CBO (+) are produced when the electron affinities of the ETL and absorber layers are different. In other words, if the position of the conduction band (CB) of the ETL is lower than the absorber, the energy cliff CBO (–) is formed at the ETL/absorber interface without the potential to act as an electron barrier.⁷⁸ So, PCBM, C_{60} , and CeO_2 have no electron barrier on the ETL/absorber interface. On the contrary, if the energy spike-CBO (+) is formed at the ETL/absorber interface it will act as an electron barrier.⁷⁸ Therefore, ETLs like TiO_2 , ZnO , IGZO, SnO_2 , and WS_2 have electron potential barriers at the ETL/absorber interface. Such kind of spike structure developed at the ETL/absorber layer interface, which can operate as a barrier for photo-generated electron flow towards the edge of the ETL/absorber, has the advantage of enhancing the photo generation of free charge carriers.

Additionally, by doing this, the rate of recombination at the contact will be reduced, improving PV performance. The primary recombination process occurs at the interface when the activation energy for carrier recombination (E_A) is lower than the bandgap of the absorber layer, as opposed to the creation of cliff structures between ETL and perovskite. Additionally, the development of “cliff-type” band alignment will lower the resistance to electron transfer, resulting in a fall in E_A , which directly influences the value of V_{OC} and, in turn, the PV parameters like J_{SC} , FF, and PCE of the solar cell.⁷⁹ The impact of CBO on V_{OC} can be described according to eqn (8) and (9) where V_{OC} denotes open circuit voltage, E_A denotes the activation energy, n denotes the diode ideality factor, K denotes Boltzmann constant, T denotes temperature, J_{00} denotes current pre factor and J_{SC} denotes short circuit current density:

$$V_{OC} = \frac{E_a}{q} - \frac{nKT}{q} \ln \frac{J_{00}}{J_{SC}} \quad (8)$$

$$E_A = E_g - CBO \quad (9)$$

3.2.5 Effect of series resistance. The performance of solar cells is significantly impacted by the shunt (R_{sh}) and series (R_s) resistances, which are produced mainly by connections among the solar cell layers, right and left side metal contacts, and manufacturing flaws.¹⁴ According to Fig. 10, the effect of R_s varied from 0–6 $\Omega\ cm^2$ while the shunt resistance was constant at $10^5\ \Omega\ cm^2$ in the case of eight double perovskites (ITO/ETL/ Cs_2BiAgI_6 /CBTS/Au) devices. During the R_s variation, PCE was decreased for all eight Cs_2BiAgI_6 perovskite device structures. The PCE value of SnO_2 , ZnO , WS_2 , and TiO_2 as ETL-based Cs_2BiAgI_6 perovskite device structure decreased from around 21.60 to 19.30%. In contrast, PCBM and IGZO as ETL-based Cs_2BiAgI_6 perovskite device structure decreased from about 20 to 19% with increasing R_s . And C_{60} and CeO_2 ETL-associated solar cell structures, showed almost 17.5 to 16% and 14.5 to 12% PCE, respectively with the increase of R_s . FF value also decreased with



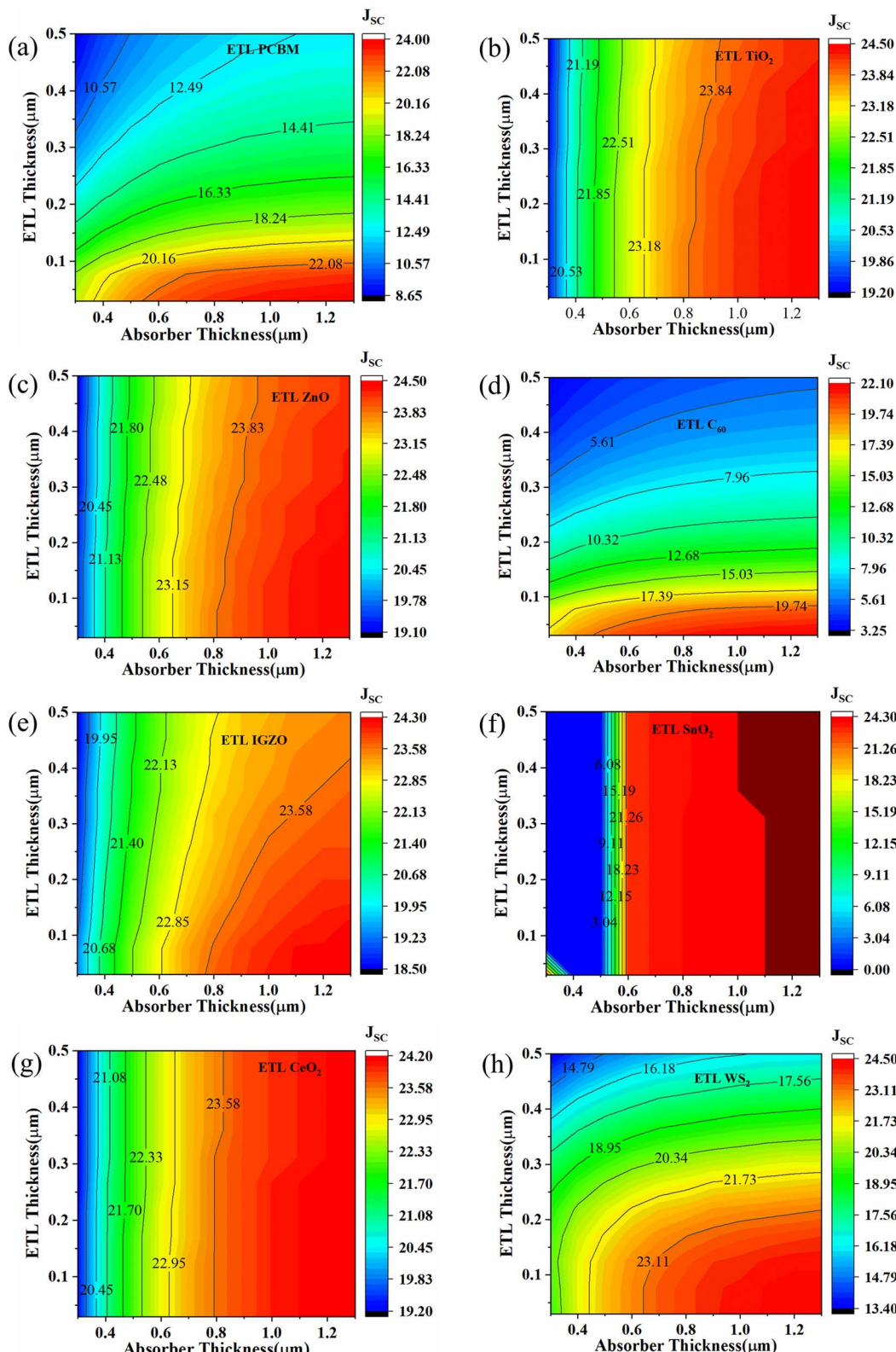


Fig. 7 Contour mapping of J_{SC} (mA cm^{-2}) when ETL as (a) PCBM, (b) TiO_2 , (c) ZnO , (d) C_60 , (e) IGZO, (f) SnO_2 , (g) CeO_2 , and (h) WS_2 .

the increase of R_S while the FF value of all ETL-associated solar cells exhibited a higher value except IGZO and CeO_2 as ETL. The J_{SC} and V_{OC} performance showed the constant value for all ETL-

associated device configurations with increasing R_S . That means R_S variation does not impact the J_{SC} and V_{OC} parameters for the studied device configurations.



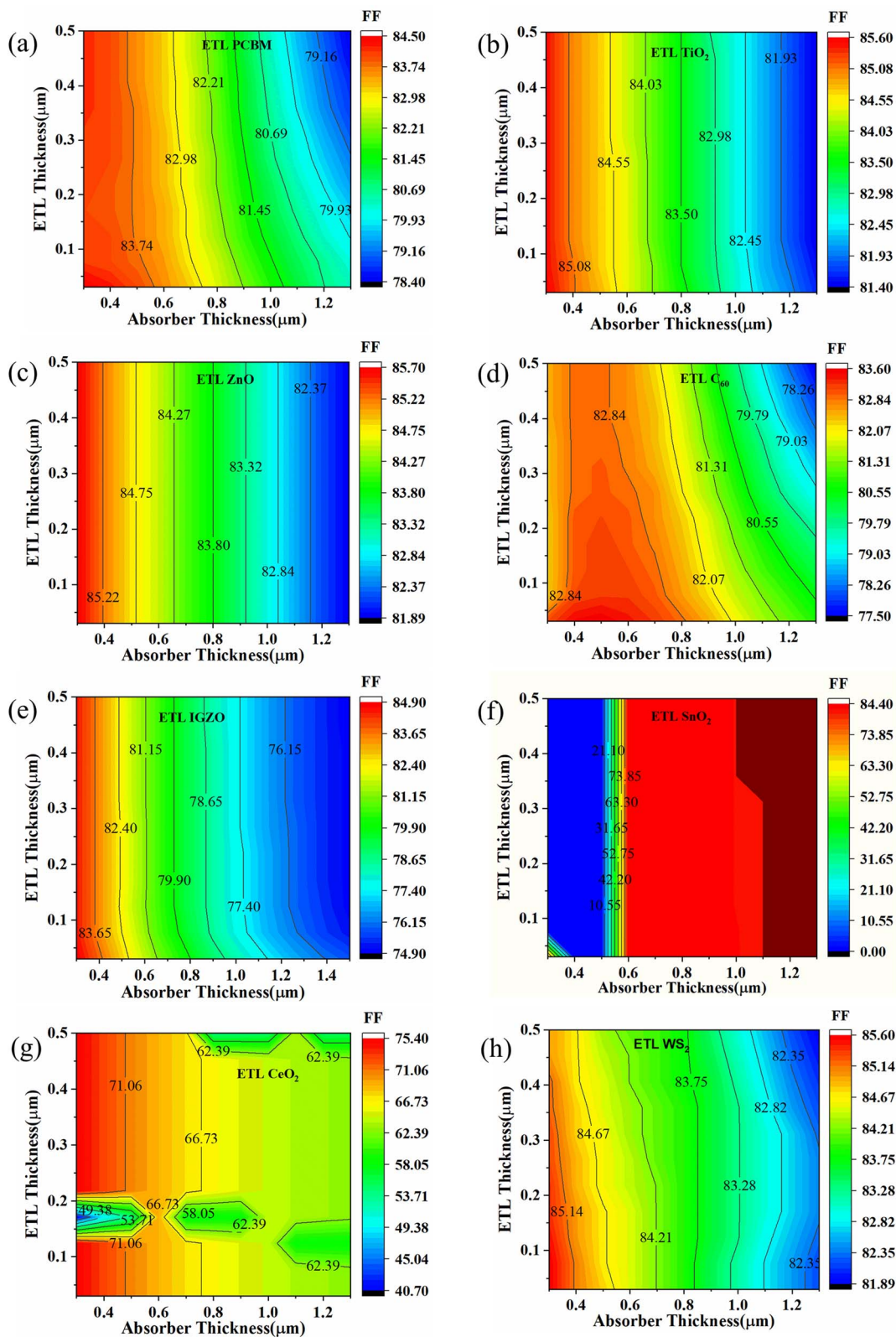


Fig. 8 Contour mapping of FF (%) when ETL as (a) PCBM, (b) TiO_2 , (c) ZnO , (d) C_{60} , (e) IGZO , (f) SnO_2 , (g) CeO_2 , and (h) WS_2 .

From Fig. 10(b) is seen that the current remains constant with the larger series resistance. $\text{CH}_3\text{NH}_3\text{SnI}_3$ -based study the performance was analyzed by varying R_s from 0 to $6 \Omega \text{ cm}^2$ while

keeping R_{sh} fixed at $10^5 \Omega \text{ cm}^2$ performed a similar trend of results where the current was unaffected by series resistance, reported by Sunny *et al.*⁸⁰ Another study reported that FAPbI_3 ,

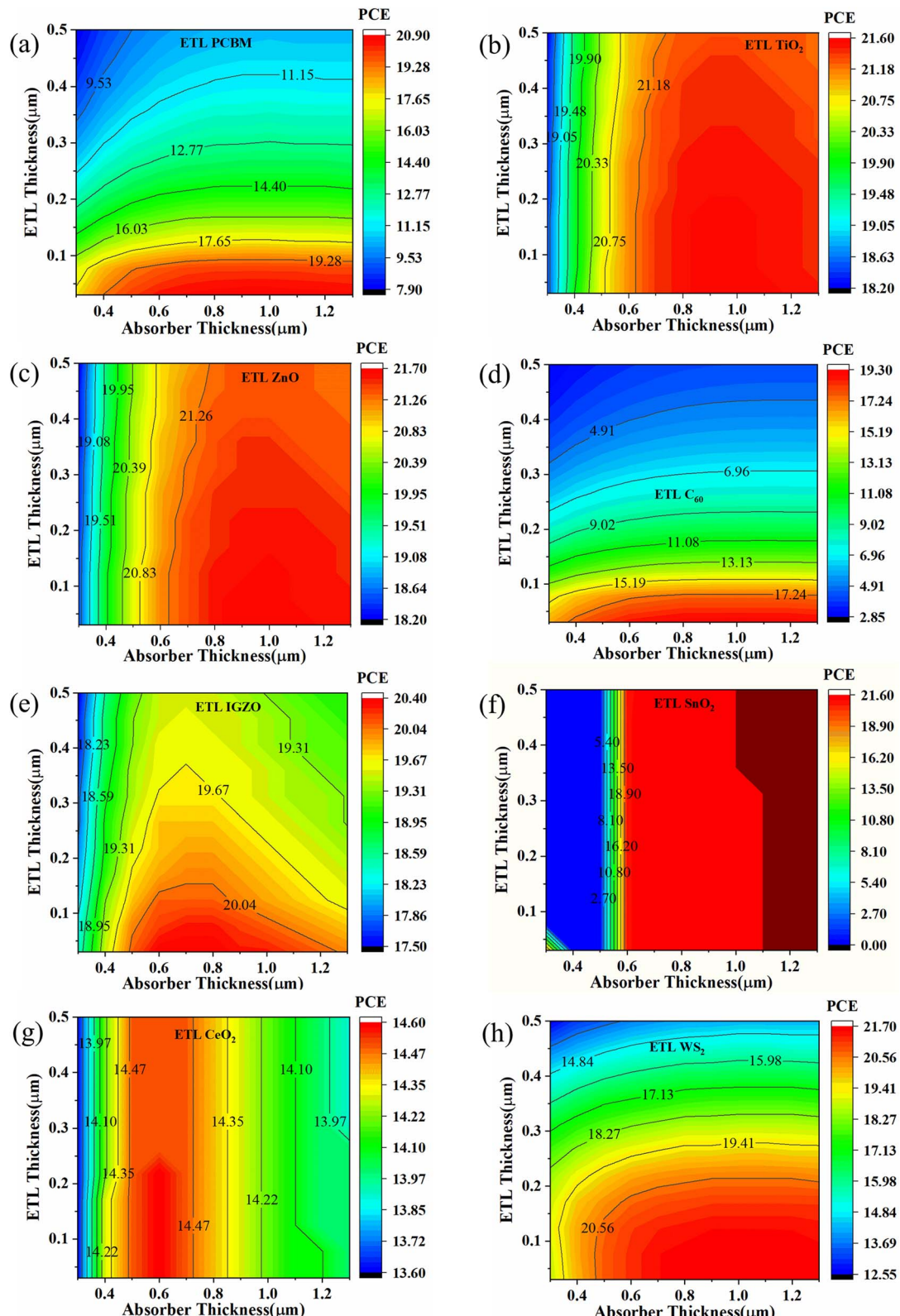


Fig. 9 Contour mapping of PCE (%) when ETL as (a) PCBM, (b) TiO_2 , (c) ZnO , (d) C_{60} , (e) IGZO , (f) SnO_2 , (g) CeO_2 , and (h) WS_2 .

$\text{FA}_{0.85}\text{Cs}_{0.15}\text{PbI}_3$, and $\text{FA}_{0.85}\text{Cs}_{0.15}\text{Pb}(\text{I}_{0.85}\text{Br}_{0.15})_3$ -based perovskites, R_S didn't affect much the current for a certain range of $30 \Omega \text{ cm}^2$. After this range, R_S of $\geq 30 \Omega \text{ cm}^2$ currents for those

particular devices tended to decline.⁸¹ R_S is the sum of resistances between various terminals like absorber, ETL, and HTL as well as the front and back contacts of the cell which doesn't



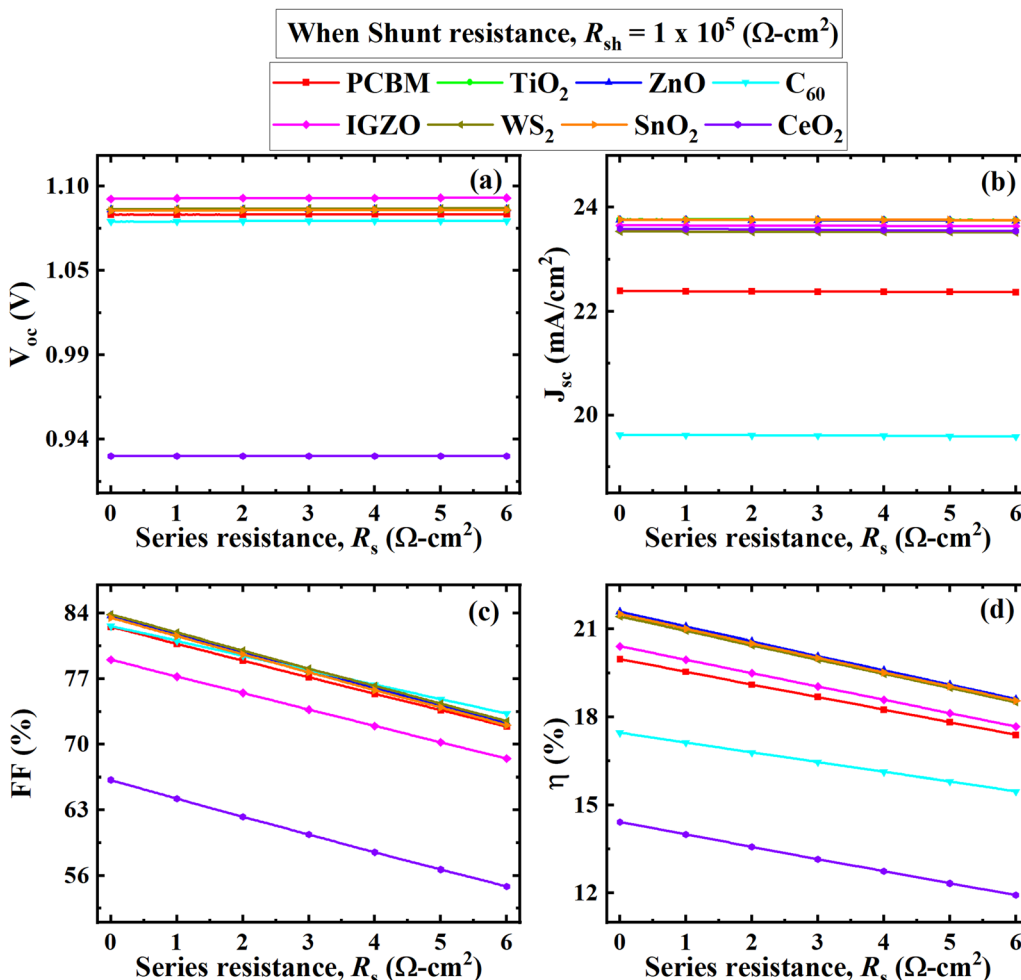


Fig. 10 Effect of R_s on performance parameters ((a) V_{OC} , (b) J_{SC} , (c) FF, and (d) PCE) of (ITO/ETL/Cs₂BiAgl₆/CBTS/Au, ETL = PCBMM, TiO₂, ZnO, C₆₀, IGZO, WS₂, SnO₂, and CeO₂) double PSCs.

affect current up to a certain range. So, it could be concluded that the current of the Cs₂BiAgl₆ perovskite was affected by various studied ETLs after the larger series of resistance above 30 Ω cm², which is in line with previous studies.

3.2.6 Effect of shunt resistance. Internal resistances, interface barriers, charge-collecting interlayers, and metal-based electrodes, are the source of R_s in PSCs, whereas leakage channels, like pinholes in the photoactive layer and recombination losses, are the source of the R_{sh} .⁸² The Shockley equation is expressed as eqn (10) and (11), describe the expected behavior of the J - V characteristic of a solar cell during ideal one-sun illumination conditions.⁸³

$$J_{SC} = J_{PH} - J_0 \left[\exp \left(\frac{q_e(V - JR_s)}{nkT_e} \right) - 1 \right] - \frac{V - JR_s}{R_{sh}} \quad (10)$$

$$V_{OC} = \left(\frac{nkT_e}{q_e} \right) \ln \left\{ \frac{J_{PH}}{J_0} \left(1 - \frac{V_{OC}}{J_{PH}R_{sh}} \right) \right\} \quad (11)$$

where, q_e is the elementary charge, J_{PH} is the photocurrent density, J_0 is the density of the reverse bias saturation current, R_s is the series resistance, R_{sh} is the shunt resistance, n is the

diode ideality factor, k is the Boltzmann constant (1.38×10^{-23} J K⁻¹), and T_e is the ambient temperature (298 K). Also, from eqn (8) and (9), it is seen that J_{SC} and V_{OC} show negative inverse relation with R_{sh} . That means with increasing R_{sh} , J_{SC} and V_{OC} 's increment happens.

The effect of V_{OC} , J_{SC} , FF, and PCE values with R_{sh} variation is visually represented in Fig. 11, where R_{sh} varied from 10^1 to 10^7 Ω cm² for all eight optimum solar cell structures. The V_{OC} , J_{SC} , FF, and PCE values showed a similar pattern with increasing shunt resistance R_{sh} . All performance parameters increased rapidly from 10^1 Ω cm² to 10^3 Ω cm² and then maintained the constant value with increasing R_{sh} . The CeO₂ as ETL associated structure showed the lowest value where CeO₂ initially increased and remained constant for V_{OC} , FF, and PCE from 0.25 V, 24%, and 2.5% to 0.9 V, 65%, and 13%, respectively, as shown in Fig. 11. In Fig. 11(b), The C₆₀ exhibited the lowest value for J_{SC} , from 18.5 to 19.5 (mA cm⁻²). The ZnO, PCBMM, TiO₂, IGZO, SnO₂, C₆₀, and WS₂ as ETL-associated solar cell structures showed an almost similar and constant value of V_{OC} , which is 1.1 V after R_{sh} of 10^3 Ω cm². The J_{SC} value of TiO₂, ZnO, IGZO, SnO₂, WS₂, and CeO₂ as ETL-associated solar cell

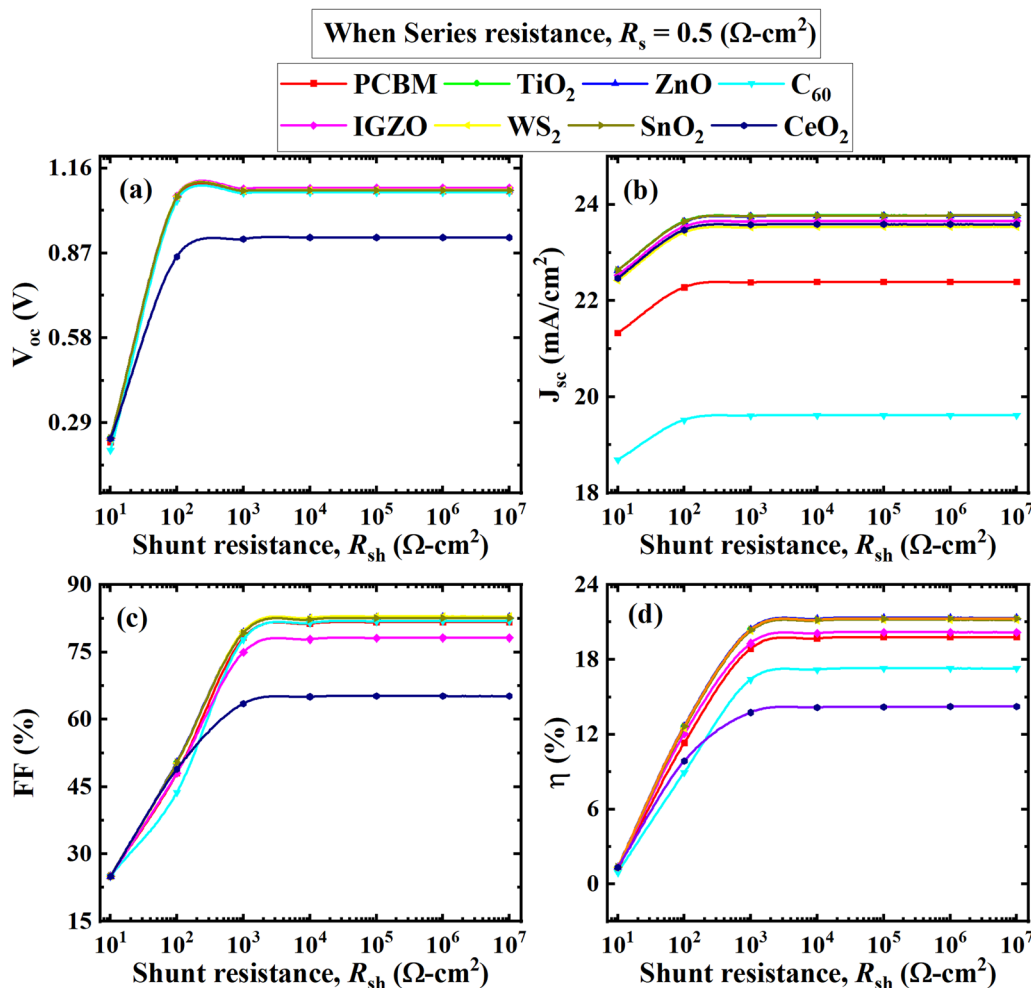


Fig. 11 Effect of R_{sh} on performance parameters ((a) V_{OC} , (b) J_{SC} , (c) FF, and (d) PCE) of (ITO/ETL/Cs₂BiAgI₆/CBTS/Au, ETL = PCBM, TiO₂, ZnO, C₆₀, IGZO, WS₂, SnO₂, and CeO₂) double PSCs.

structure showed 21.0 (mA cm^{-2}) initially and then increased to 23.5 (mA cm^{-2}) and remained constant (Fig. 11(b)).

3.2.7 Effect of temperature. One of the most important factors in determining the stability of solar cell performance is having a thorough understanding of solar cell performance at high operating temperatures. Due to the distortion between layers at high temperatures, the performance of the majority of solar cell architectures exhibits instability. Recent studies on perovskites-based optoelectronics have shown improvements in the device's performance stability at high temperatures.^{84–86} The temperature range has been adjusted from 275 K to 475 K to investigate the relationship between temperature and the efficiency of the solar cell. Fig. 12(a), (c), and (d) shows PCE, FF, and V_{OC} values are decreased with increasing temperature for almost all optimum solar cell structures.

In contrast, J_{SC} remained almost constant for all optimum device configurations with temperature variation (Fig. 12(b)). The C₆₀ as an ETL-associated solar cell showed a lower J_{SC} of 20 mA cm^{-2} . The PCBМ as an ETL-associated structure demonstrated almost 22 mA cm^{-2} of J_{SC} value, which is higher than the C₆₀. The other ETLs with device configurations exhibited

around 23.5 mA cm^{-2} of J_{SC} value with increasing temperature. The V_{OC} value was decreased from 1.16 to 0.70 V with increasing temperature for all studied device configurations except CeO₂ as ETL associated device, which decreased from 0.92 to 0.72 V (Fig. 12(a)). The FF value decreased from around 85 to 74% for all optimum device configurations except IGZO and CeO₂ ETL-associated devices. The PCE decreased for all devices with the increasing temperature. However, the V_{OC} value decreased for all optimum device configurations with increasing temperature due to the inverse relationship between V_{OC} , and the reversed saturation current density, J_0 . The J_0 increased at a higher temperature. Eqn (12) shows the relation between V_{OC} and J_0 .

$$V_{OC} = \frac{Ak'T_1}{q} \left[\ln \left(1 + \frac{J_{SC}}{J_0} \right) \right] \quad (12)$$

where, $\frac{k'T_1}{q}$ stands for the thermal voltage, and A stands for the ideality factor.

In addition, when the temperature of the PSC rises, the flaws become worse, and the V_{OC} value decrease which is consistence with previous studies.¹⁴ From Fig. 12(b), it is evident that the



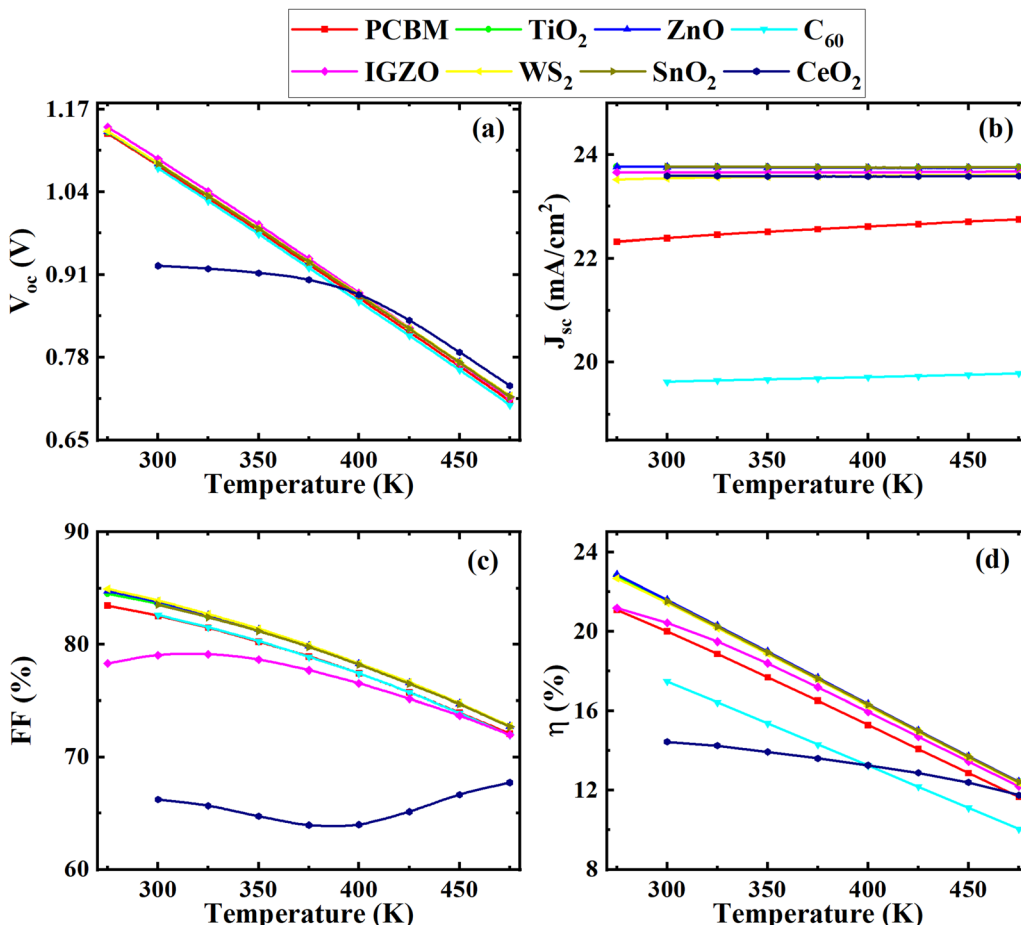


Fig. 12 Effect of temperatures on performance parameters ((a) V_{OC} , (b) J_{SC} , (c) FF, and (d) PCE) of (ITO/ETL/Cs₂BiAgI₆/CBTS/Au, ETL = PCBM, TiO₂, ZnO, C₆₀, IGZO, WS₂, SnO₂, and CeO₂) double PSCs.

current was affected slightly due to the reduction of bandgap with the increase in temperature. But the range of change is very marginal which seems to be constant during the increment of temperature. And, CH₃NH₃SnI₃ perovskite showed a similar kind of trend of change in current with an increase in temperature from 260 K to 473 K.⁸⁰ In these circumstances, the bandgap reduction could be less of being double perovskite such kind of a slight current change for temperature change.

3.2.8 Effect of capacitance and Mott-Schottky. Fig. 13(a) and (b) show the Mott-Schottky (M-S) plots and the plots of capacitance per unit area (C) with bias voltage (V), respectively, for eight suitable solar cells. The built-in voltage (V_{bi}) and charge carrier density (N_d) can be extracted from $C-V$ measurements by using the well-known M-S analysis experimental method. It is used in traditional semiconductor devices that contain p-n and semiconductor/metal junctions with fixed depletion layers and space charge regions. Eqn (13) yields the junction capacitance per area (C) value.

$$\frac{1}{C^2} = \frac{2\epsilon_0\epsilon_r}{qN_d}(V_{bi} - V) \quad (13)$$

Here, ϵ_0 is the vacuum permittivity, ϵ_r is the donor's dielectric constant, q is the electronic charge, and V is the applied voltage (Fig. 13(b)).^{87,88} N_d is generated from the gradient of the linear

component, and V_{bi} is generated from an extension of the linear part to the voltage axis. The CeO₂ ETL-associated device shows voltage-independent capacitance from -0.4 V to 0.5 V, and an exponentially increasing pattern has been shown after 0.5 V (Fig. 13(a)). Whereas other ETL-associated solar structures represent the independent voltage capacitance it may be because of the saturation of depletion layer capacitance, as seen in Fig. 13(a). In the case of CeO₂ as ETL associated structure V_{bi} shows declining in nature where ZnO, C₆₀, PCBM, SnO₂, TiO₂, and WS₂ as ETL associated structure shows a higher voltage.

3.2.9 Effect of generation and recombination rate. Fig. 13(c) and (d) show the generation and recombination rates, respectively. The electron-hole pairs are created during the carrier generation process when an electron is excited from the valence band to the conduction band, producing a hole in the valence band. The emission of electrons and holes brings on carrier generation. To determine the creation of electron-hole pairs $G(x)$, SCAPS-1D employs the incident photon flux $N_{phot}(-\lambda, x)$. From this photon flux for each position and wavelength, the value of $G(x)$ can be computed through eqn (14).

$$G(\lambda, x) = \alpha(\lambda, x)N_{phot}(\lambda, x) \quad (14)$$



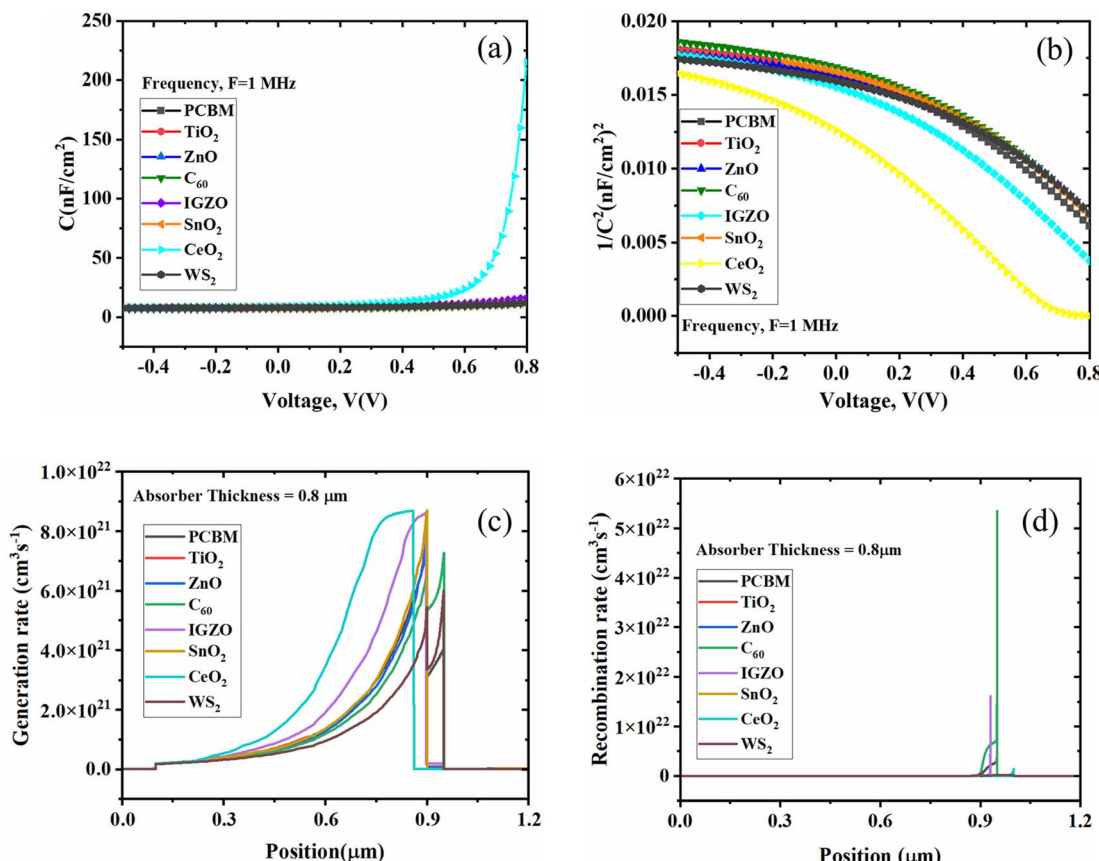


Fig. 13 (a) Capacitance (C), (b) Mott–Schottky ($1/C^2$) plot, (c) generation rate, and (d) recombination rate for eight studied structures.

The process of recombination is the opposite of the process of generation, in which the electrons and holes of the conduction band are coupled and annihilated. The charge carrier's lifespan and density determine the solar cell's recombination rate. First, the electron–hole recombination is decreased because of the defect states present within the absorber layer. Then, the energy states are produced, which impacts the electron–hole recombination profile within the solar cell structure. Due to flaws and grain boundaries, the recombination rate distribution is not uniform, as shown in Fig. 13(d).⁵⁴

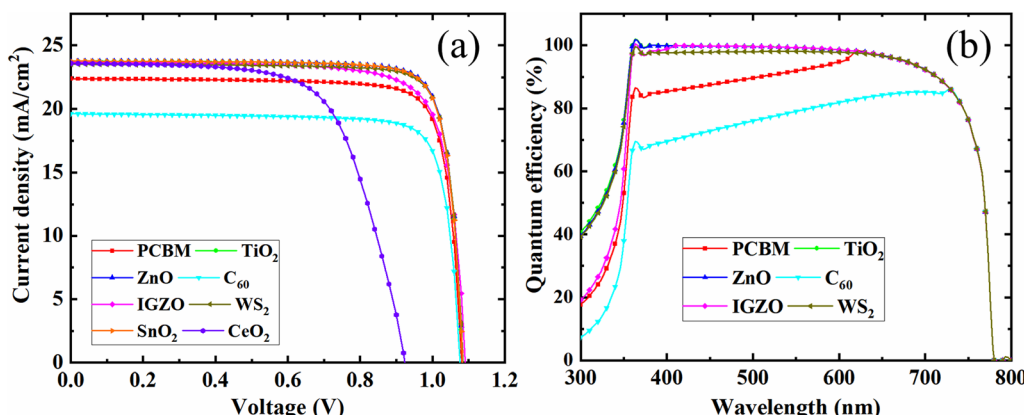


Fig. 14 (a) J – V characteristics and (b) QE curve of the double PSCs.

3.2.10 J – V and QE characteristics. Fig. 14(a) shows the J – V characteristics changing pattern of the studied eight solar cell structures. According to Fig. 14(a), it is noticed that C_{60} as an ETL-associated PSC showed about $19\ \text{mA cm}^{-2}$ as current density, while the V_{OC} is more significant than one volt. However, CeO_2 as an ETL-associated device exhibited a J_{SC} of about $23\ \text{mA cm}^{-2}$ although the V_{OC} was less than $1.0\ \text{V}$. However, the other ETLs associated structures showed better performance than C_{60} and CeO_2 as ETL-associated device structures. The ZnO as ETL-associated structure demonstrated



23 mA cm⁻² with unity open circuit voltage density, as shown in Fig. 14(a). The defect amount in perovskite films is a critical factor in determining the device's performance since the photoelectrons are produced in these layers. However, the electron–hole recombination behaviors are essential in defining the photovoltaic parameters of the PSC. The *J*–*V* curve in a perovskite film is shown in Fig. 14(a) as a function of bulk trap density. All photovoltaic parameters are drastically reduced when defect states are present in perovskite films. This is consistent with the observation that significant crystallinity in perovskite reduces charge recombination and enhances performance.⁴⁴

Fig. 14(b) shows the quantum efficiency (QE) curve with respect to a different wavelength. The C₆₀ as ETL with PSC showed the optimum QE of 80% when the wavelength was almost 700 nm. The optimum QE of PCBM as an ETL-associated solar cell structure exhibited around 95% at around 620 nm. In addition, the other four ETL-associated PSCs demonstrated the highest QE of around 100% at 350 nm. Fig. 14(b) shows that the six sets of PSCs do not have QE above 800 nm. However, because of recombination, where charge carriers cannot pass into an external circuit, the QE for most solar cells is decreased. The QE is impacted by the same processes that impact collection probability. For instance, altering the front surface might impact carriers produced close to the surface. Free carrier absorption, which lowers QE in longer wavelengths, may also be brought on by highly doped front surface layers.⁸⁹

3.3 Comparison with wxAMPS simulation results and previous work

3.3.1 Comparison between SCAPS-1D and wxAMPS results. A comparison of Cs₂BiAgI₆-based double perovskite solar cells is conducted in this section. Table 5 gives a comparative view of the performance parameters of eight Cs₂BiAgI₆ base solar cell structures found by optimizing different ETL and HTL from numerous simulations. PCBM as ETL associated with Cs₂BiAgI₆-based perovskite solar structure shows 19.99% of PCE in SCAPS-

1D simulator whereas 20.70% of PCE in wxAMPS simulator (Table 5). In addition, TiO₂ as ETL associated with Cs₂BiAgI₆-based solar cells shows 21.55% of PCE while 23.06% of PCE in the wxAMPS simulator. ZnO as an ETL-associated solar cell structure shows 21.59% PCE when SCAPS-1D is used, whereas wxAMPS shows 22.04% PCE. Similarly, C₆₀, IGZO, SnO₂, CeO₂, and WS₂ as ETL-associated Cs₂BiAgI₆-based solar cell structures show 17.47%, 20.41%, 21.52%, 14.44%, 21.43% of PCE in SCAPS-1D simulator however in wxAMPS simulator, the PCE values show 21.03%, 22.38%, 21.93%, —, 21.23%. In the case of V_{OC}, PCBM as an ETL-associated structure shows 1.08 V in the SCAPS-1D simulator. In contrast, in the wxAMPS simulator, the device structure shows 1.18 V. Like PCBM as ETL associated structure, both simulator shows similar pattern results for V_{OC} for all device configurations. In addition, the performance parameters *J*_{SC} and FF in SCAPS-1D and wxAMPS simulator show the closest pattern for all device structures. Comparing the performance parameters of the eight solar cell structures, SCAPS-1D and wxAMPS simulators show the nearest results except for PCE and V_{OC}, where wxAMPS shows a little higher result than SCAPS-1D (Table 5). The obtained performance parameters result from both simulators help us to understand the charges transport layers and absorber materials that are suitable for device configuration. Since both simulators give the closest performance results for eight sets of optimum solar device configurations, the presented results are reliable for further investigation which is consistent with previous studies.^{40,90}

3.3.2 Comparison of SCAPS-1D results with previous work.

Table 6 compares the performance parameters of the presented eight device configurations with recently published optimum configurations. Table 6 shows that the presented optimum Cs₂-BiAgI₆ double perovskite-based solar cell shows a higher PCE value than the previously published Cs₂BiAgX₆ device structure. Presented eight sets of device structures PCE are 19.99%, 21.55%, 21.59%, 20.42%, 21.52%, 21.43%, 17.47%, and 14.44% whereas previously published device structures such as FTO/PCBM/Cs₂BiAgI₆/PTAA/Au structure shows almost 16.23% PCE,⁷²

Table 5 Comparison between SCAPS 1D and wxAMPS software simulation

Device structure	Software	V _{OC} (V)	J _{SC} (mA cm ⁻²)	FF (%)	PCE (%)
ITO/PCBM/Cs ₂ BiAgI ₆ /CBTS/Au	SCAPS-1D	1.08	22.39	82.56	19.99
	wxAMPS	1.18	20.86	84.21	20.70
ITO/TiO ₂ /Cs ₂ BiAgI ₆ /CBTS/Au	SCAPS-1D	1.08	23.8	83.61	21.55
	wxAMPS	1.18	23.00	84.69	23.06
ITO/ZnO/Cs ₂ BiAgI ₆ /CBTS/Au	SCAPS-1D	1.085	23.76	83.78	21.59
	wxAMPS	1.18	21.97	84.81	22.04
ITO/C ₆₀ /Cs ₂ BiAgI ₆ /CBTS/Au	SCAPS-1D	1.07	19.62	82.65	17.47
	wxAMPS	1.18	21.09	84.73	21.03
ITO/IGZO/Cs ₂ BiAgI ₆ /CBTS/Au	SCAPS-1D	1.09	23.65	79.04	20.42
	wxAMPS	1.19	22.87	82.02	22.38
ITO/SnO ₂ /Cs ₂ BiAgI ₆ /CBTS/Au	SCAPS-1D	1.08	23.76	83.54	21.52
	wxAMPS	1.18	21.94	82.62	21.93
ITO/CeO ₂ /Cs ₂ BiAgI ₆ /CBTS/Au	SCAPS-1D	0.92	23.59	66.21	14.44
	wxAMPS	—	—	—	—
ITO/WS ₂ /Cs ₂ BiAgI ₆ /CBTS/Au	SCAPS-1D	1.08	23.53	83.91	21.43
	wxAMPS	1.18	21.16	84.94	21.23



Table 6 The comparison of PV parameters of $\text{Cs}_2\text{BiAgI}_6$ and similar absorbers-based solar cells

Type ^a	Device structure	V_{OC} (V)	J_{SC} (mA cm ⁻²)	FF (%)	PCE (%)	Year	Ref.
E	FTO/c-TiO ₂ /mTiO ₂ /Cs ₂ AgBiBr ₆ /N719/spiro-OMeTAD/Ag	1.06	5.13	—	2.84	2020	92
E	FTO/TiO ₂ /Cs ₂ AgBiBr ₆ /spiro-OMeTAD/Au	0.98	3.96	62.40	2.43	2021	91
T	FTO/PCBM/Cs ₂ BiAgI ₆ /PTAA/Au	1.08	19.94	74.87	16.23	2021	72
T	Ohmic contact/spiro-OMeTAD/Cs ₂ BiAgI ₆ /TiO ₂ /SnO ₂ :F(ZnO ₂)/ohmic contact	1.18	16.2	80.20	15.90	2018	93
T	Glass/FTO/TiO ₂ /Cs ₂ AgBiBr ₆ /Cu ₂ O/Au	1.5	11.45	42.10	7.25	2020	90
T	ZnO-NR/Cs ₂ AgBiBr ₆ /P3HT(base)	0.91	11.10	44.02	4.48	2021	40
T	ITO/PCBM/Cs ₂ BiAgI ₆ /CBTS/Au	1.08	22.39	82.56	19.99	—	^b
T	ITO/TiO ₂ /Cs ₂ BiAgI ₆ /CBTS/Au	1.08	23.8	83.61	21.55	—	^b
T	ITO/ZnO/Cs ₂ BiAgI ₆ /CBTS/Au	1.08	23.76	83.78	21.59	—	^b
T	ITO/C ₆₀ /Cs ₂ BiAgI ₆ /CBTS/Au	1.07	19.62	82.65	17.47	—	^b
T	ITO/IGZO/Cs ₂ BiAgI ₆ /CBTS/Au	1.09	23.65	79.04	20.42	—	^b
T	ITO/SnO ₂ /Cs ₂ BiAgI ₆ /CBTS/Au	1.08	23.76	83.54	21.52	—	^b
T	ITO/CeO ₂ /Cs ₂ BiAgI ₆ /CBTS/Au	0.92	23.59	66.21	14.44	—	^b
T	ITO/WS ₂ /Cs ₂ BiAgI ₆ /CBTS/Au	1.08	23.53	83.91	21.43	—	^b

^a E = experimental, T = theoretical. ^b This work.

FTO/TiO₂/Cs₂BiAgI₆/spiro-OMeTAD/Au structure shows around 2.43% PCE.⁹¹ The V_{OC} values of the presented solar structures are compatible with published device configurations. In contrast, the J_{SC} and FF values of the presented solar structure are higher than those of the previously published Cs₂BiAgX₆-base device structure. All presented solar structure shows J_{SC} of greater than 19 mA cm⁻², whereas earlier published device structure shows the lowest J_{SC} value except FTO/PCBM/Cs₂BiAgI₆/PTAA/Au structure. Table 6 shows that the presented eight solar structures are shown more effective performance than the previously reported Cs₂BiAgX₆-based solar cells.

The first 2 solar cell device structures of Table 6 used a different absorber, *i.e.*, Cs₂AgBiBr₆ (which shows less than 3% efficiency) than our studied absorber, *i.e.*, Cs₂BiAgI₆. Up till now, the research on photovoltaics using a Cs₂BiAgI₆ absorber has been unique which was different from the experimental studied Cs₂BiAgBr₆ absorber-based solar cells. Our studied absorbers' characteristics like thickness, bandgap, acceptor, defect density, *etc.* varied from the previous theoretical and experimental studies of device structures. At the same time, our studied ETLs, and HTLs are not matched with previously studied experimental ones as per their properties as well. Furthermore, optical properties also vary from absorber to absorber which leads to solar energy absorption. The studied Cs₂BiAgI₆ absorber had better optical properties which were evident from the performance of 16.23% of PCE in the case of FTO/PCBM/Cs₂BiAgI₆/PTAA/Au structure reported by Srivastava *et al.*⁷² From all the above reasons, we can conclude that our studied Cs₂AgBiBr₆ solar cell shows better PCE than other studied similar solar absorbers, *i.e.*, Cs₂AgBiBr₆ based different structured solar cells.

4 Summary

This work concludes a combined DFT, SCAPS-1D, and wxAMPS based study to design, investigate and optimize Cs₂BiAgI₆ double perovskite-based solar cells. Both the band structure and density of states *via* DFT analyses confirm the semi-conducting nature of Cs₂BiAgI₆ material. The bonding nature of

Cs-I and Ag-I bonds is found to be ionic, while it is a covalent Bi-I bond. Moreover, the analysis of optical properties suggests the possible application of this double perovskite in solar cells. In the next step, Cs₂BiAgI₆-based double perovskite solar cell configurations are investigated with ninety-six combinations of solar cell structures using eight ETLs and twelve HTLs through SCAPS-1D simulation. The Cs₂BiAgI₆ absorber layer-based device with CBTS as HTL delivered 19.99%, 21.55%, 21.59%, 17.47%, 20.42%, 21.52%, 14.44%, and 21.43% PCE with PCBM, TiO₂, ZnO, C₆₀, IGZO, SnO₂, CeO₂, WS₂ ETL respectively. After a comparison of various characteristics among these eight best-optimized configurations, the following findings are summarized:

(1) Among all studied combinations, TiO₂, ZnO, and SnO₂ ETLs-associated devices showed comparatively better PCE of ~21.5% with CBTS HTL due to its suitable band alignment.

(2) From the effect of absorber and ETL thickness, it is evident that SnO₂ and WS₂ ETLs-associated devices can deliver ~21.5% of PCE.

(3) ITO/ZnO/Cs₂BiAgI₆/CBTS/Au PSC showed a considerable decline of PCE while series resistance increased to 6 Ω cm².

(4) In the case of shunt resistance, the performance of ITO/ZnO/Cs₂BiAgI₆/CBTS/Au structure is better in comparison with other devices.

(5) While the temperature increased from 275 K to 475 K the performance of the ZnO ETL-associated structure is the best among all devices.

(6) V_{OC} , and J_{SC} were almost independent with respect to R_s , and J_{SC} also remained unaffected with temperature.

(7) For capacitance and Mott-Schottky characteristics, CeO₂ and C₆₀ ETLs-associated devices showed relatively maximum PCE at 0.8 V for a voltage sweep from -0.4 V to 0.8 V.

(8) Also, CeO₂ and C₆₀ ETLs associated devices showed the highest generation and recombination rates at 0.9 and 1 μm respectively.

(9) ZnO ETL device showed better $J-V$ and QE characteristics due to its suitable band alignment in comparison with other ETLs associated devices.



(10) Comparing SCAPS-1D results with wxAMPS results, it is evident that the difference between all the devices is marginal, which might help to understand the accuracy of the work.

Extensive numerical simulations reported in this work can be extended to other perovskite materials to study the potential perovskite absorber materials for solar cell applications, followed by development using device simulators. This can help the experimentalists to synthesize the desired material with the most efficient device architecture.

Data availability

The raw/processed data required to reproduce these findings cannot be shared at this time as the data also forms part of an ongoing study.

Author contributions

M. K. Hossain: conceptualization, methodology, software, validation, formal analysis, investigation, data curation, writing – original draft, writing – review & editing, supervision, project administration; A. A. Arnab: formal analysis, investigation, data curation, writing – original draft; R. C. Das: writing – review & editing; K. M. Hossain: writing – original draft; M. H. K. Rubel: software, data curation; formal analysis, investigation, writing – review & editing; M. F. Rahman: writing – review & editing; H. Bencherif: writing – review & editing; M. E. Emetere: writing – review & editing; Mustafa K. A. Mohammed: writing – review & editing; R. Pandey: writing – review & editing.

Conflicts of interest

The authors declare that they have no known competing financial interests or personal relationships that could have appeared to influence the work reported in this paper.

Acknowledgements

This research did not receive any specific grant from funding agencies in the public, commercial, or not-for-profit sectors. The SCAPS-1D program was provided by Dr M. Burgelman of the University of Gent in Belgium. The authors would like to express their gratitude to him. They would also like to thank Professor A. Rockett and Dr Yiming Liu from UIUC, as well as Professor Fonash from Penn State University, for their contributions to the wxAMPS program. We also acknowledge G. F. Ishraque Toki of Donghua University, Shanghai, China for reviewing the manuscript.

References

- 1 H. Tang, S. He and C. Peng, *Nanoscale Res. Lett.*, 2017, **12**, 410.
- 2 M. K. Nazeeruddin, *Nature*, 2016, **538**, 463–464.
- 3 M. F. Rahman, M. J. A. Habib, M. H. Ali, M. H. K. Rubel, M. R. Islam, A. B. M. Ismail and M. K. Hossain, *AIP Adv.*, 2022, **12**, 105317.
- 4 M. M. M. Islam, A. Kowsar, A. K. M. M. Haque, M. K. Hossain, M. H. Ali, M. H. K. Rubel and M. F. Rahman, *Process Integr. Optim. Sustain.*, 2022, DOI: [10.1007/s41660-022-00294-8](https://doi.org/10.1007/s41660-022-00294-8).
- 5 M. K. Hossain, S. M. K. Hasan, M. I. Hossain, R. C. Das, H. Bencherif, M. H. K. Rubel, M. F. Rahman, T. Emrose and K. Hashizume, *Nanomaterials*, 2022, **12**, 3581.
- 6 M. K. Hossain, G. A. Raihan, M. A. Akbar, M. H. Kabir Rubel, M. H. Ahmed, M. I. Khan, S. Hossain, S. K. Sen, M. I. E. Jalal and A. El-Denglawey, *ACS Appl. Electron. Mater.*, 2022, **4**, 3327–3353.
- 7 M. K. Hossain, M. H. K. Rubel, M. A. Akbar, M. H. Ahmed, N. Haque, M. F. Rahman, J. Hossain and K. M. Hossain, *Ceram. Int.*, 2022, **48**, 32588–32612.
- 8 M. K. Hossain, R. Chanda, A. El-Denglawey, T. Emrose, M. T. Rahman, M. C. Biswas and K. Hashizume, *Ceram. Int.*, 2021, **47**, 23725–23748.
- 9 A. Kojima, K. Teshima, Y. Shirai and T. Miyasaka, *J. Am. Chem. Soc.*, 2009, **131**, 6050–6051.
- 10 Y. Chen, L. Zhang, Y. Zhang, H. Gao and H. Yan, *RSC Adv.*, 2018, **8**, 10489–10508.
- 11 C. O. Ramírez Quiroz, Y. Shen, M. Salvador, K. Forberich, N. Schrenker, G. D. Spyropoulos, T. Heumüller, B. Wilkinson, T. Kirchartz, E. Specker, P. J. Verlinden, X. Zhang, M. A. Green, A. Ho-Baillie and C. J. Brabec, *J. Mater. Chem. A*, 2018, **6**, 3583–3592.
- 12 K. Yoshikawa, H. Kawasaki, W. Yoshida, T. Irie, K. Konishi, K. Nakano, T. Uto, D. Adachi, M. Kanematsu, H. Uzu and K. Yamamoto, *Nat. Energy*, 2017, **2**, 17032.
- 13 N. Kumar, J. Rani and R. Kurchania, *Sol. Energy*, 2021, **221**, 197–205.
- 14 M. K. Hossain, M. H. K. Rubel, G. F. I. Toki, I. Alam, M. F. Rahman and H. Bencherif, *ACS Omega*, 2022, **7**(47), 43210–43230.
- 15 Y. Raoui, H. Ez-Zahraouy, S. Ahmad and S. Kazim, *Sustainable Energy Fuels*, 2021, **5**, 219–229.
- 16 A. Babayigit, A. Ethirajan, M. Muller and B. Conings, *Nat. Mater.*, 2016, **15**, 247–251.
- 17 I. R. Benmessaoud, A.-L. Mahul-Mellier, E. Horváth, B. Maco, M. Spina, H. A. Lashuel and L. Forró, *Toxicol. Res.*, 2016, **5**, 407–419.
- 18 A. Babayigit, D. Duy Thanh, A. Ethirajan, J. Manca, M. Muller, H.-G. Boyen and B. Conings, *Sci. Rep.*, 2016, **6**, 18721.
- 19 H. Bencherif and M. Khalid Hossain, *Sol. Energy*, 2022, **248**, 137–148.
- 20 H. Bencherif, F. Meddour, M. H. Elshorbagy, M. K. Hossain, A. Cuadrado, M. A. Abdi, T. Bendib, S. Kouda and J. Alda, *Micro Nanostruct.*, 2022, **171**, 207403.
- 21 O. A. Lozhkina, A. A. Murashkina, M. S. Elizarov, V. V. Shilovskikh, A. A. Zolotarev, Y. V. Kapitonov, R. Kevorkyants, A. V. Emeline and T. Miyasaka, *Chem. Phys. Lett.*, 2018, **694**, 18–22.
- 22 R. E. Brandt, R. C. Kurchin, R. L. Z. Hoye, J. R. Poindexter, M. W. B. Wilson, S. Sulekar, F. Lenahan, P. X. T. Yen, V. Stevanović, J. C. Nino, M. G. Bawendi and T. Buonassisi, *J. Phys. Chem. Lett.*, 2015, **6**, 4297–4302.



23 H. Zhou, Q. Chen, G. Li, S. Luo, T. Song, H.-S. Duan, Z. Hong, J. You, Y. Liu and Y. Yang, *Science*, 2014, **345**, 542–546.

24 F. Giustino and H. J. Snaith, *ACS Energy Lett.*, 2016, **1**, 1233–1240.

25 F. Jiang, D. Yang, Y. Jiang, T. Liu, X. Zhao, Y. Ming, B. Luo, F. Qin, J. Fan, H. Han, L. Zhang and Y. Zhou, *J. Am. Chem. Soc.*, 2018, **140**, 1019–1027.

26 E. T. McClure, M. R. Ball, W. Windl and P. M. Woodward, *Chem. Mater.*, 2016, **28**, 1348–1354.

27 P.-K. Kung, M.-H. Li, P.-Y. Lin, J.-Y. Jhang, M. Pantaler, D. C. Lupascu, G. Grancini and P. Chen, *Sol. RRL*, 2020, **4**, 1900306.

28 K. Dave, M. H. Fang, Z. Bao, H. T. Fu and R. S. Liu, *Chem. - Asian J.*, 2020, **15**, 242–252.

29 C. Frangville, M. Rutkevičius, A. P. Richter, O. D. Velev, S. D. Stoyanov and V. N. Paunov, *ChemPhysChem*, 2012, **13**, 4235–4243.

30 P. K. Nayak, D. T. Moore, B. Wenger, S. Nayak, A. A. Haghaghirad, A. Fineberg, N. K. Noel, O. G. Reid, G. Rumbles, P. Kukura, K. A. Vincent and H. J. Snaith, *Nat. Commun.*, 2016, **7**, 13303.

31 F. Marchetti, E. Moroni, A. Pandini and G. Colombo, *J. Phys. Chem. Lett.*, 2021, **12**, 3724–3732.

32 A. H. Slavney, T. Hu, A. M. Lindenberg and H. I. Karunadasa, *J. Am. Chem. Soc.*, 2016, **138**, 2138–2141.

33 W. Ning, F. Wang, B. Wu, J. Lu, Z. Yan, X. Liu, Y. Tao, J.-M. Liu, W. Huang, M. Fahlman, L. Hultman, T. C. Sum and F. Gao, *Adv. Mater.*, 2018, **30**, 1706246.

34 G. Volonakis, M. R. Filip, A. A. Haghaghirad, N. Sakai, B. Wenger, H. J. Snaith and F. Giustino, *J. Phys. Chem. Lett.*, 2016, **7**, 1254–1259.

35 F. Igbari, Z. K. Wang and L. S. Liao, *Adv. Energy Mater.*, 2019, **9**, 1–32.

36 X.-G. Zhao, D. Yang, J.-C. Ren, Y. Sun, Z. Xiao and L. Zhang, *Joule*, 2018, **2**, 1662–1673.

37 H. Absike, N. Baaalla, R. Lamouri, H. Labrim and H. Ez-zahraouy, *Int. J. Energy Res.*, 2022, **46**, 11053–11064.

38 H. Wu, A. Erbing, M. B. Johansson, J. Wang, C. Kamal, M. Odelius and E. M. J. Johansson, *ChemSusChem*, 2021, **14**, 4507–4515.

39 N. Singh, A. Agarwal and M. Agarwal, *Opt. Mater.*, 2021, **114**, 110964.

40 I. Alam, R. Mollick and M. A. Ashraf, *Phys. B*, 2021, **618**, 413187.

41 J. Gong, S. B. Darling and F. You, *Energy Environ. Sci.*, 2015, **8**, 1953–1968.

42 H. Choi, S. Park, S. Paek, P. Ekanayake, M. K. Nazeeruddin and J. Ko, *J. Mater. Chem. A*, 2014, **2**, 19136–19140.

43 C. Devi and R. Mehra, *J. Mater. Sci.*, 2019, **54**, 5615–5624.

44 M. Liu, M. B. Johnston and H. J. Snaith, *Nature*, 2013, **501**, 395–398.

45 M. K. Hossain, M. T. Rahman, M. K. Basher, M. S. Manir and M. S. Bashar, *Optik*, 2019, **178**, 449–460.

46 M. K. Hossain, M. T. Rahman, M. K. Basher, M. J. Afzal and M. S. Bashar, *Results Phys.*, 2018, **11**, 1172–1181.

47 M. K. Hossain, A. A. Mortuza, S. K. Sen, M. K. Basher, M. W. Ashraf, S. Tayyaba, M. N. H. Mia and M. J. Uddin, *Optik*, 2018, **171**, 507–516.

48 M. K. Hossain, M. F. Pervez, M. N. H. Mia, A. A. Mortuza, M. S. Rahaman, M. R. Karim, J. M. M. Islam, F. Ahmed and M. A. Khan, *Results Phys.*, 2017, **7**, 1516–1523.

49 M. K. Hossain, M. F. Pervez, M. J. Uddin, S. Tayyaba, M. N. H. Mia, M. S. Bashar, M. K. H. Jewel, M. A. S. Haque, M. A. Hakim and M. A. Khan, *Mater. Sci.*, 2017, **36**, 93–101.

50 M. K. Hossain, M. F. Pervez, M. N. H. Mia, S. Tayyaba, M. J. Uddin, R. Ahamed, R. A. Khan, M. Hoq, M. A. Khan and F. Ahmed, *Mater. Sci.*, 2017, **35**, 868–877.

51 M. K. Hossain, M. F. Pervez, S. Tayyaba, M. J. Uddin, A. A. Mortuza, M. N. H. Mia, M. S. Manir, M. R. Karim and M. A. Khan, *Mater. Sci.*, 2017, **35**, 816–823.

52 Y. Raoui, H. Ez-zahraouy, N. Tahiri, O. El, S. Ahmad, S. Kazim, O. El Bounagui, S. Ahmad and S. Kazim, *Sol. Energy*, 2019, **193**, 948–955.

53 S. Z. Haider, H. Anwar and M. Wang, *Semicond. Sci. Technol.*, 2018, **33**, 035001.

54 M. H. K. Rubel, M. A. Hossain, M. K. Hossain, K. M. Hossain, A. A. Khatun, M. M. Rahaman, M. Ferdous Rahman, M. M. Hossain and J. Hossain, *Results Phys.*, 2022, **42**, 105977.

55 M. H. K. Rubel, S. K. Mitro, M. K. Hossain, K. M. Hossain, M. M. Rahaman, J. Hossain, B. K. Mondal, A. Akter, M. F. Rahman, I. Ahmed and A. K. M. A. Islam, *Mater. Today Commun.*, 2022, **33**, 104302.

56 M. I. Kholil, M. T. H. Bhuiyan, M. A. Rahman, M. S. Ali and M. Aftabuzzaman, *AIP Adv.*, 2021, **11**, 035229.

57 M. Roknuzzaman, K. Ostrikov, H. Wang, A. Du and T. Tesfamichael, *Sci. Rep.*, 2017, **7**, 14025.

58 J. Ur Rehman, M. Usman, S. Amjid, M. Sagir, M. Bilal Tahir, A. Hussain, I. Alam, R. Nazir, H. Alrobei, S. Ullah and M. Ali Assiri, *Comput. Theor. Chem.*, 2022, **1209**, 113624.

59 M. A. Hadi, M. N. Islam and J. Podder, *RSC Adv.*, 2022, **12**, 15461–15469.

60 J. Zhou, X. Rong, M. S. Molokeev, X. Zhang and Z. Xia, *J. Mater. Chem. A*, 2018, **6**, 2346–2352.

61 M. D. Segall, P. J. D. Lindan, M. J. Probert, C. J. Pickard, P. J. Hasnip, S. J. Clark and M. C. Payne, *J. Phys.: Condens. Matter*, 2002, **14**, 2717–2744.

62 M. C. Payne, M. P. Teter, D. C. Allan, T. A. Arias and J. D. Joannopoulos, *Rev. Mod. Phys.*, 1992, **64**, 1045–1097.

63 D. Vanderbilt, *Phys. Rev. B: Condens. Matter Mater. Phys.*, 1990, **41**, 7892–7895.

64 J. P. Perdew, K. Burke and M. Ernzerhof, *Phys. Rev. Lett.*, 1996, **77**, 3865–3868.

65 H. J. Monkhorst and J. D. Pack, *Phys. Rev. B: Condens. Matter Mater. Phys.*, 1976, **13**, 5188–5192.

66 T. H. Fischer and J. Almlöf, *J. Phys. Chem.*, 1992, **96**, 9768–9774.

67 Z. Boekelheide, T. Saerbeck, A. P. J. Stampfl, R. A. Robinson, D. A. Stewart and F. Hellman, *Phys. Rev. B: Condens. Matter Mater. Phys.*, 2012, **85**, 094413.



68 S. S. Hussain, S. Riaz, G. A. Nowsherwan, K. Jahangir, A. Raza, M. J. Iqbal, I. Sadiq, S. M. Hussain and S. Naseem, *J. Renewable Energy*, 2021, **2021**, 1–12.

69 F. Liu, J. Zhu, J. Wei, Y. Li, M. Lv, S. Yang, B. Zhang, J. Yao and S. Dai, *Appl. Phys. Lett.*, 2014, **104**, 253508.

70 Y. Liu, Y. Sun and A. Rockett, *Sol. Energy Mater. Sol. Cells*, 2012, **98**, 124–128.

71 J. He, T. Zhang, P. Tang, C. Qiu, X. Feng and X. Luo, *Electrochim. Acta*, 2014, **125**, 218–224.

72 S. Srivastava, A. K. Singh, P. Kumar and B. Pradhan, *J. Appl. Phys.*, 2022, **131**, 175001.

73 M. H. K. Rubel, K. M. Hossain, S. K. Mitro, M. M. Rahaman, M. A. Hadi and A. K. M. A. Islam, *Mater. Today Commun.*, 2020, **24**, 100935.

74 W.-C. Hu, Y. Liu, D.-J. Li, X.-Q. Zeng and C.-S. Xu, *Comput. Mater. Sci.*, 2014, **83**, 27–34.

75 J. Zhou, Z. Xia, M. S. Molokeev, X. Zhang, D. Peng and Q. Liu, *J. Mater. Chem. A*, 2017, **5**, 15031–15037.

76 A. H. Reshak, V. V. Atuchin, S. Auluck and I. V. Kityk, *J. Phys.: Condens. Matter*, 2008, **20**, 325234.

77 T. Kim, J. Lim and S. Song, *Energies*, 2020, **13**, 5572.

78 Y. Raoui, H. Ez-Zahraouy, S. Kazim and S. Ahmad, *J. Energy Chem.*, 2021, **54**, 822–829.

79 Z. Selssabil and S. Baya, Dissertation of Master, Study of electron transport effect on perovskite solar cells using simulation, University Mohamed Khider de Biskra, 2019.

80 A. Sunny, S. Rahman, M. M. Khatun and S. R. Al Ahmed, *AIP Adv.*, 2021, **11**, 065102.

81 S. Karthick, S. Velumani and J. Bouclé, *Sol. Energy*, 2020, **205**, 349–357.

82 K. Tvingstedt, L. Gil-Escriv, C. Momblona, P. Rieder, D. Kiermasch, M. Sessolo, A. Baumann, H. J. Bolink and V. Dyakonov, *ACS Energy Lett.*, 2017, **2**, 424–430.

83 Y. Li, B. Ding, Q.-Q. Chu, G.-J. Yang, M. Wang, C.-X. Li and C.-J. Li, *Sci. Rep.*, 2017, **7**, 46141.

84 Y. Li, Z. Shi, L. Lei, F. Zhang, Z. Ma, D. Wu, T. Xu, Y. Tian, Y. Zhang, G. Du, C. Shan and X. Li, *Chem. Mater.*, 2018, **30**, 6744–6755.

85 Z. Ma, Z. Shi, C. Qin, M. Cui, D. Yang, X. Wang, L. Wang, X. Ji, X. Chen, J. Sun, D. Wu, Y. Zhang, X. J. Li, L. Zhang and C. Shan, *ACS Nano*, 2020, **14**, 4475–4486.

86 Z. Shi, S. Li, Y. Li, H. Ji, X. Li, D. Wu, T. Xu, Y. Chen, Y. Tian, Y. Zhang, C. Shan and G. Du, *ACS Nano*, 2018, **12**, 1462–1472.

87 S. Lin, *Bell Syst. Tech. J.*, 1965, **44**, 2245–2269.

88 M. Fischer, K. Tvingstedt, A. Baumann and V. Dyakonov, *ACS Appl. Energy Mater.*, 2018, **1**, 5129–5134.

89 S. C. Baker-Finch, K. R. McIntosh, D. Yan, K. C. Fong and T. C. Kho, *J. Appl. Phys.*, 2014, **116**, 063106.

90 M. T. Islam, M. R. Jani, S. M. Al Amin, M. S. U. Sami, K. M. Shorowordi, M. I. Hossain, M. Devgun, S. Chowdhury, S. Banerje and S. Ahmed, *Opt. Mater.*, 2020, **105**, 109957.

91 M. S. Shadabroo, H. Abdizadeh and M. R. Golobostanfar, *ACS Appl. Energy Mater.*, 2021, **4**, 6797–6805.

92 X. Yang, Y. Chen, P. Liu, H. Xiang, W. Wang, R. Ran, W. Zhou and Z. Shao, *Adv. Funct. Mater.*, 2020, **30**, 2001557.

93 B. Smith, *Efficient Lead-Free Perovskite Solar Cell*, Urbana, IL 61801, USA, 2018.

